이학박사 학위논문

Plasmonically Enhanced Optical and Chemical Properties of Noble Metal Nanostructures for SERS-Based Bioassay and Catalytic Chemical Reaction Monitoring

광학적 및 화학적 특성이 향상된 귀금속 나노구조체의 플라즈모닉 특성 연구와 이의 표면증강라만산란 기반 바이오분석 및 촉매화학 반응 응용

2020 년 8 월

서울대학교 대학원

화학부 무기화학

고 성 민

Plasmonically Enhanced Optical and Chemical Properties of Noble Metal Nanostructures for SERS-Based Bioassay and Catalytic Chemical Reaction Monitoring

광학적 및 화학적 특성이 향상된 귀금속 나노구조체의 플라즈모닉 특성 연구와 이의 표면증강라만산란 기반 바이오분석 및 촉매화학 반응 응용

지도교수 남 좌 민

이 논문을 이학박사 학위논문으로 제출함

2020 년 8 월

서울대학교 대학원

화학부 무기화학

고 성 민

고성민의 박사학위논문을 인준함

2020 년 8 월

위 원 장 _____(인)

부 위 원 장 _____(인)

위 원 _____(인)

위 원 _____(인)

위 원 _____(인)

Abstract

Plasmonically Enhanced Optical and Chemical Properties of Noble Metal Nanostructures for SERS-Based Bioassay and Catalytic Chemical Reaction Monitoring

Sung Min Ko

Department of Chemistry

The Graduate School

Seoul National University

Surface-enhanced Raman scattering (SERS) has been received tremendous attention due to the unique properties enabling a strong enhancement of an electromagnetic (EM) field at the vicinity of the surface of noble metal (e.g., gold, silver, and copper) nanostructures. Therefore, the SERS technique is highly promising for the chemical and biological sensing/imaging applications because it can allow for high sensitivity, selectivity, multiplexity, and long-term stability in optical signals. The highly strong enhancement of the EM field can exhibit an ultrasensitive detection limit

even at the single-molecule level, and depend on the size, shape, composition, material, etc. Importantly, the plasmonic coupling at the nanometer-sized small gap between plasmonic nanostructures can affect significantly to the overall EM field enhancement. For this reason, lots of attempts have been conducted to enhance the EM field near the plasmonic nanostructures by forming a nanogaps; however, the precise control for nanostructure-assembly and nanogap formation to generate strong SERS signals is highly challenging, especially in terms of a quantitative manner.

Together with the optical utilization of plasmonic metal nanostructures for enhancing EM field near the surface of nanostructures, plasmonically enhanced chemical properties under laser irradiation have been also intensively studied. When highly excited and energetic hot electrons, generated by the non-radiative decay process of a localized surface plasmon, are transferred (i.e., injected) to the adjacent reactants, it allows hot electron to involve and promote the catalytic chemical reaction in terms of reaction efficiency and selectivity. Up to now, many studies have proved that hot electrons can participate in various chemical reactions and lead to efficiency of target chemical reaction; however, kinetic and quantitative analysis of how much do the hot electrons improve and boost the rate of catalytic chemical reactions has been rarely conducted, yet.

In this thesis, plasmonically enhanced optical and chemical properties of noble metal nanostructures are presented. In addition, the plasmonic properties of as-synthesized metallic nanostructures are investigated in optical and chemical aspects. For the SERS-based bioassay, DNA-mediated hierarchic assembly of Au nanocubes are investigated; and

bimetallic nanoparticles consisting of silver (Ag) and platinum (Pt) are utilized for the catalytic chemical reaction monitoring and improvement of conversion rate constant.

In chapter 1, a hierarchic-nanocube-assembly-based SERS (H-Cube-SERS) bioassay to controllably amplify the electromagnetic field between gold nanocubes (AuNCs) is presented. Based on this strategy, H-Cube-SERS assay allows for detecting target DNA with a wide dynamic range from 100 aM to 10 pM concentrations in a stable and reproducible manner. It is also found that the uniformly formed AuNCs with flat surfaces are much more suitable for highly sensitive, reliable and quantitative bio-detection assays due to faster DNA binding kinetics, sharper DNA melting transition, wider hot spot regions and less dependence on light polarization direction than spherical Au nanoparticles with curved interfaces.

In chapter 2, a bimetallic nanoparticle consisting of Ag and Pt (Ag/Pt NP) for SERS-signal-based real-time monitoring of catalytic chemical reaction is presented. The bimetallic Ag/Pt NPs exhibiting optical/plasmonic properties (from Ag) and catalytic properties (from Pt) simultaneously in the single nanostructure are synthesized through a galvanic replacement reaction between Pt ions and cuboidal Ag nanoshell structure (cuboidal AgNS). By controlling the degree of galvanic replacement reaction the atomic ratio of Ag and Pt are adjusted, and the catalytic performance (i.e., conversion rate constant) of the resulting Ag/Pt nanocatalysts are evaluated under laser illumination. Interestingly, the conversion rate constant of Ag/Pt NPs showed unusual trend in catalytic reaction, that is, the less Pt loading the faster chemical reaction. It is

expected that this unusual catalytic tendency might be caused by the highly energetic hot electron transfer process from plasmonic Ag nanostructure to the adjacent reactant binding onto the Ag/Pt NPs under laser irradiation, which eventually involved in the chemical reaction. This suggests that the generation and injection of hot electron can contribute significantly to the overall catalytic chemical reaction as an additional electron source, resulting in an improvement of the catalytic conversion rate constant even with very low loadings of Pt.

Comprehensively, these works pave the pathways to the quantitative and sensitive bio-detection on a SERS platform that can be extended to other assembly systems, and open avenues in designing of efficient plasmonic catalysts and versatile hot-electron-engineering for efficient bimetallic photocatalysts.

Key words: Plasmonics, Surface-Enhanced Raman Scattering (SERS), Gold Nanocube, DNA, Hierarchic Assembly, SERS-Based Bioassay, Hot electron, Silver/Platinum Bimetallic Nanostructure, Galvanic Replacement Reaction, Catalytic Chemical Reaction Monitoring, Kinetic Analysis, Improvement of conversion rate constant.

Student Number: 2015-30975

Contents

List of Figures

Chapter 1

Chapter 2

List of Tables

Chapter 1

Chapter 1

Hierarchic Interfacial Nanocube Assembly for Sensitive, Selective and Quantitative DNA Detection with Surface-Enhanced Raman Scattering

1.1. Introduction

Surface-enhanced Raman scattering (SERS) is mainly based on the enhancement of the electromagnetic (EM) field on the surface or within the gap of noble metal nanostructures (typically, gold (Au) and silver nanoparticles), and is highly promising in chemical and biological sensing and imaging because of its ultrahigh sensitivity, signal selectivity, multiplexing potential and long-term signal stability.[1-4] Enhancing the EM field, which is the key to increasing the sensitivity of SERS-based assays, can allow for detecting even at the single-molecule level,[5,6] and depends on the morphology, composition and assembly of noble metal structure substrates.[7-11] Enhancement in the EM field can be significantly affected by plasmonic coupling within the nanometer-sized gap between plasmonic nanostructures,[12,13] and, in this regard, various plasmonic nanogap-based bio-detection strategies have been reported.[14-20] However, precise assembly control and interparticle gap engineering with reproducible and reliable SERS signals remain highly challenging.[21-26]

Among assembled nanostructures with strong plasmonic coupling, metal nanocube-assembled clusters (e.g., Au nanocube dimers) can yield more stable and reproducible SERS signals than other structures such as spherical particles.[27,28] For example, when spherical nanoparticles are assembled, the EM field is enhanced only at the highly localized center of the assembled area because of their convex surface structures (point-to-point coupling). Further, although the plasmonic coupling within a very small hot-spot area is highly intense, the degree of plasmonic coupling for nanosphere dimers decreases sharply as a particle or a Raman dye moves away from the

center of the assembled area. Thus, the enhancement largely varies and results in unreliable and non-quantitative SERS signals in many cases. On the other hand, the enhancement in the EM field between nanocubes is relatively uniform and stable and occurs over a wider region of the assembled clusters because of the flat surface structure of the nanoparticles (facet-to-facet coupling).[27,28] Therefore, precisely shaped and sized Au nanocubes can be highly suitable as building blocks for assembling and forming plasmonically enhanced SERS signals for the development of highly sensitive and quantitative SERS-based biosensors.

Herein, I employed a controlled hierarchic Au nanocube (AuNC) assembly strategy with precisely synthesized AuNC building blocks in developing a highly sensitive and reliable SERS bioassay for detecting DNA [hierarchic-nanocube-assembly-based SERS (H-Cube-SERS) assay, **Figure 1.1**]. To detect target DNA strands, first, the target DNA strands were captured by the DNA-modified magnetic microparticles (DNA-MMPs) and the target-capturing Au nanocubes (TC-AuNCs) via a sandwich-type hybridization (target-capturing step), which resulted in the formation of a TC-AuNC-MMP complex (NC-complex-**1**). Here, the oligonucleotides attached on the TC-AuNCs were modified by Raman molecules (Cy3 in this case), which were located near the surfaces of the TC-AuNCs. Next, the signal-amplifying Au nanocubes (SA-AuNCs) were directly hybridized on the surfaces of the TC-AuNCs linked to NC-complex-**1** (signal-amplifying step), resulting in the formation of a SA-AuNC-TC-AuNC-MMP complex (NC-complex-**2**). Details of the DNA sequences used here are given in **Table 1.1**. In the case of NC-complex-**1**, the SERS signal intensity was not

strong enough for detecting low concentrations of the target DNA because of the lack of plasmonic coupling- based EM field enhancements between AuNCs. In the case of the assembled AuNC cluster forms (NC-complex-**2**), the SERS signal was highly enhanced because of the multiple plasmonic couplings at the assembled areas of the AuNC clusters, resulting in a highly improved detection limit. Importantly, I found that DNA strands on the flat surfaces of AuNCs can facilitate hybridization of target DNA with other DNA-modified AuNCs in a more efficient manner, resulting in faster binding kinetics and sharper melting transitions than DNA-modified Au nanospheres (AuNSs). H-Cube-SERS assay allows for reliably detecting DNA with a dynamic range from 100 aM to 10 pM concentrations with a good reproducibility (standard deviations: 8.3–15.6 %). Our strategy and method pave the pathways to efficient and controlled formation of assembled plasmonic nanostructures and the development of highly sensitive, quantitative SERS bioassays.

1.2. Experimental Section

Reagents and materials

Magnetic microparticles (Dynabeads® MyOne™ Carboxylic Acid, average diameter of 1 μm) were purchased from Invitrogen Dynal AS (Oslo, Norway). HPLC-purified oligonucleotides were purchased from IDT, Inc (Coralville, IA, USA). Gold(III) chloride trihydrate ($HAuCl_4 \cdot 3H_2O$, ≥99.9%), cetyltrimethylammonium bromide (CTAB), benzyldimethylhexadecylammonium chloride (BDAC), L-ascorbic acid (AA, ≥99.9%), DL-dithiothreitol (DTT, ≥99.0%), sodium dodecyl sulfate (SDS, ≥98.5%), 2-(*N*-morpholino)ethanesulfonic acid (MES, ≥99.0%), *N*-(3-dimethylaminopropyl)-*N'*-ethylcarbodiimide hydrochloride (EDC, commercial grade), ethylenediaminetetraacetic acid (EDTA, 99.4-100.06%), potassium cyanide (KCN, ≥96.0%), and Tween®-20 were purchased from Sigma-Aldrich (St. Louis, MO, USA). Cetyltrimethylammonium chloride (CTAC) was purchased from Tokyo Chemical Industry Co., Ltd. (Tokyo, Japan). Sodium borohydride ($NaBH_4$, 97.0%) and sodium bromide (NaBr, ≥99.0%) were purchased from DAEJUNG Chemicals & Metals Co. (Siheung, Gyeonggi, Korea) and Samchun Pure Chemical Co. (Pyungtack, Gyeonggi, Korea), respectively. All the chemical reagents were used as received without further purification. In all experiments, NANOpure water (Millipore, Milli-Q 18.2 MQ.cm) was used.

Synthesis of 50-nm-sized Au nanospheres (AuNSs)

The AuNSs were synthesized using the seed-mediated growth method with a minor modification.[29] To prepare the 50-nm-sized AuNSs, the synthesis were performed the following three steps:

1. Synthesis of CTAB-capped Au seeds

Aqueous solutions of CTAB (200 mM, 5 mL) and $HAuCl_4 \cdot 3H_2O$ (0.5 mM, 5 mL) were mixed in a 50-mL round-bottom flask at 27 °C under magnetic stirring (300 rpm). A freshly prepared aqueous $NaBH_4$ solution (10 mM, 0.6 mL) was quickly injected into the flask, after which the mixture turned brown immediately. The reaction mixture was stirred for 3 min at 300 rpm and then incubated at 27 °C for 3 h without agitation.

2. Synthesis of 10-nm-sized Au nanospheres

To obtain 10-nm-sized AuNSs, 50 μL of the CTAB-capped Au clusters was introduced into a mixture of CTAC (200 mM, 2 mL) and AA (100 mM, 1.5 mL) solution. This was following by the rapid injection of an aqueous $HAuCl_4 \cdot 3H_2O$ solution (0.5 mM, 2 mL) into the reaction mixture, which was then stirred for 15 min at 27 °C under magnetic stirring (300 rpm). The product was washed with distilled water once by centrifugation at 20,000 ×*g* for 30 min and then dispersed in a CTAC solution (20 mM, 1 mL) for further use.

3. Synthesis of 50-nm-sized Au nanospheres

An aqueous $HAuCl_4 \cdot 3H_2O$ solution (0.5 mM, 2 mL) was injected into a mixture of CTAC (100 mM, 2 mL), AA (10 mM, 130 μL), and the 10-nm-sized AuNSs (6 μL) using a syringe pump with an injection rate of 2 $mL \cdot h^{-1}$. During the injection of the $HAuCl_4 \cdot 3H_2O$ solution, the reaction mixture was

stirred continuously (500 rpm) at 27 °C. The resulting solution was washed twice with distilled water by centrifugation at 4,000 ×*g* for 5 min.

Synthesis of 50-nm-sized Au nanocubes (AuNCs)

The AuNCs were synthesized using the seed-mediated growth method with a minor modification.[28] To obtain 50-nm-sized AuNCs, an aqueous solution of CTAC (100 mM, 6 mL), NaBr (20 mM, 30 μL), and AA (10 mM, 390 μL) were mixed in 20 mL vial at 27 °C under continuous stirring (500 rpm). Next, 10 μL of the 10-nm-sized Au nanospheres (3.9 O.D.) was introduced into the above mixture. This was followed by a single injection of an aqueous $HAuCl_4 \cdot 3H_2O$ solution (0.5 mM, 6 mL). The reaction mixture was stirred for 25 min at 500 rpm and then left undisturbed for 1 h at 27 °C. The product was washed twice with distilled water by centrifugation (4,000 ×*g* for 5 min), and the final volume was adjusted to 1 mL. To obtain a high yield of the AuNCs, I performed a purification step according to a previously reported method with a modification.[30] First, the synthesized 50-nm-sized AuNCs were dispersed in a CTAB solution, whose final concentration was adjusted to 1 mM. Next, 100 μL of this dispersion of AuNCs dispersed in CTAB was mixed with 100 μL of a BDAC solution (180 mM), and the resulting mixture was left undisturbed overnight at 30 °C. Finally, the supernatants were discarded carefully, and the pellets were washed twice with distilled water by centrifugation (4,000 ×*g* for 5 min).

Preparation of DNA-modified magnetic microparticles (DNA-MMPs)

The DNA-MMPs were prepared according to the company's instructions with a minor modification. An amine-functionalized oligonucleotide (DNA sequence: 5′-NH_2-A_{10}-PEG_6-AGAAAGAGGAGTTAA-3′) was attached to the MMPs, which were coated with the carboxyl functional group, via EDC coupling. Typically, 200 μL of the MMP solution (10 $mg \cdot mL^{-1}$) was washed twice with a 100 mM MES buffer (pH 4.8) and redispersed in 20 μL of the MES buffer. Next, 10 μL of an amine-functionalized oligonucleotide (1 mM) and 10 μL of a 1 M EDC solution in MES buffer were added to the MMP solution. The mixture was shaken for 4 h at room temperature. The DNA-modified MMPs were then washed three times with a washing buffer (250 mM, Tris pH 8.0, 0.01% Tween®-20), and suspended in 200 μL of a Tris-EDTA buffer (10 mM, Tris pH 8.0, 1 mM EDTA).

Preparation of DNA-modified AuNCs and AuNSs

To prepare the TC-probes (TC-AuNC and TC-AuNS), I attached fluorophore (Cy3)-labeled DNA strands (DNA sequence: 5′-TCCATGCAACTCTAA-A_{10}-Cy3-SH-3′) on the surfaces of 50-nm-sized AuNCs and AuNSs using the salt-aging method with a minor modification.[31] Before introducing the DNA strands on the AuNCs and AuNSs, the synthesized 50-nm-sized AuNCs and AuNSs were washed three times with a 0.1% (wt/vol) SDS solution. First, disulfide-modified oligonucleotides were reduced by a 0.1 M DTT solution in a 0.17 M phosphate buffer (pH 8.0) and purified with a desalting NAP-5 column (Sephadex™ G-25 DNA Grade, GE Healthcare, UK). Excess amounts of the purified oligonucleotides (2×10^5 times the number of nanoparticles) were

added to the solution of the 50-nm-sized nanoparticles (AuNCs and AuNSs), and the mixtures were incubated overnight at room temperature. The resulting solutions were adjusted to obtain a final phosphate concentration of 10 mM (pH 7.4), and an SDS concentration of 0.1% (wt/vol). The solutions were then shaken gently for 1 h at room temperature. The mixtures were then adjusted to obtain a 0.3 M NaCl solution by adding six aliquots of a salting solution (2 M NaCl, 10 mM PB, 0.1% SDS) every hour. During the salt-aging procedure, the mixtures were incubated in a water bath at 60 °C to minimize the nonspecific interactions of the DNA on the Au surface. After the salting step, the mixtures were incubated overnight at room temperature. The mixtures were then centrifuged at 4,000 ×*g* for 5 min, and the supernatants were removed carefully. The precipitates were redispersed in a 0.3 M phosphate-buffered saline solution (PBSS) (10 mM PB, 0.3 M NaCl, 0.01% SDS, pH 7.4) buffer. This washing step was repeated twice. To prepare the SA-probes (SA-AuNC and SA-AuNS), I simply replaced the DNA strand (DNA sequence: 5′-TTAGAGTTGCATGGA-A_{10}-SH-3′) during the procedure to prepare the TC-probes.

Quantification of DNA-loading capacity of 50-nm-sized AuNCs and AuNSs

To determine the number of DNA strands attached on the surfaces of the Au nanoprobes, fluorophore (Cy3)-labeled DNA strands were used to prepare the DNA-modified AuNCs and AuNSs (TC-AuNCs and TC-AuNSs). A KCN solution was mixed with the solutions of the TC-AuNCs and TC-AuNSs, and the mixtures were heated at 90 °C for 5 min to dissolve the TC-

probes; the final concentration of KCN was 100 mM while the particle concentrations were 11.7 and 10.2 pM for the TC-AuNCs and TC-AuNSs, respectively. The fluorescence emission intensity of the released Cy3-modified DNA strands was measured using a fluorophotometer ($\lambda_{excitation}$ = 546 nm and $\lambda_{emission}$ = 560 nm). The number of attached DNA strands was calculated from a standard curve obtained using the same DNA in known concentrations (**Figure 1.2**).

Structure-dependent DNA binding kinetics

To evaluate the structure-dependent DNA binding kinetics during the formation of NC- and NS-complex-**1** (target-capturing step in **Figure 1.1**), DNA-MMPs (10 mg·mL^{-1}, 1 μL) were added to the solution of HAV DNA (1 nM, 100 μL) and incubated for 1 h; here, six reaction samples were prepared to monitor the number of unbound nanoprobes as a function of the hybridization time. The unbound HAV DNA strands were removed under a magnetic force, and the resulting solution was washed three times with 0.3 M phosphate-buffered saline solution (PBSS) (10 mM PB, 0.3 M sodium chloride, 0.01% (wt/vol) sodium dodecyl sulfate, pH 7.4) buffer. Next, the prepared solution of the TC-probes (3 pM, 60 μL) was added to each reaction sample, and the mixtures were incubated for different hybridization times. At a certain hybridization time (0, 5, 10, 15, 20, and 25 min), a magnet collected the NC- and NS-complex-**1**. Immediately, the extinction spectrum of the supernatant of each reaction sample (which contained the unbound TC-probes) was measured to monitor the number of unbound TC-probes. To evaluate the structure-dependent DNA binding kinetics during

the formation of NC- and NS-complex-**2** (signal-amplifying step in **Figure 1.1**), I simply modified the procedure for monitoring the binding kinetics of the TC-probes. Briefly, 100 μL of HAV DNA (1 nM), 1 μL of the DNA-MMPs (10 $mg \cdot mL^{-1}$), and 60 μL of the TC-probes (2 pM) were used to form NC- and NS-complex-**1**. The resulting complexes were then washed three times with 0.3 M PBSS buffer. Next, the solutions of the SA-AuNCs and SA-AuNSs (6 pM, 60 μL) were added to the prepared NC-complex-**1** and NS-complex-**1** solutions, respectively. The extinction spectra of the unbound SA-probes were measured at different hybridization times (0, 10, 20, 30, 40, 50, and 60 min).

Melting transition measurements to evaluate structure-dependent dissociation of nanoprobe aggregates

To prepare the nanoprobe aggregates, 3 pM of the TC-probes and SA-probes (2 mL) were allowed to hybridize at room temperature for 4 h. As the two probes hybridized, the resulting mixture turned colorless, indicating the formation of the nanoprobe aggregates. The temperature-induced dissociations of the clusters (melting transitions) were evaluated by monitoring the change in the intensity of the extinction peak of the dissociating nanoprobes as the temperature of the solution was increased from 25 to 85 °C. The melting temperatures ($\boldsymbol{T_m}$) of the AuNC and AuNS aggregates were determined from the temperature corresponding to the maximum of the first-order derivative of the dissociation curve.

Hierarchic-nanocube-assembly-based SERS bioassay for detecting DNA

For the DNA detection assay, the sandwich-hybridization method was performed using the DNA-MMPs, target DNA strands, the TC-AuNCs, and the SA-AuNCs. First, solutions of the target DNA (hepatitis A virus; HAV, DNA sequence: 5′-TTAGAGTTGCATGGATTAACTCCTCTTTCT-3′) with different concentrations (100 aM to 10 pM) were prepared using 0.3 M PBSS buffer. Further, 10 pM of a non-complementary DNA (hepatitis B virus; HBV, DNA sequence: 5′-TTGGCTTTCAGTTATATGGATGATGTGGTA-3′) was used as the control. Next, 1 μL of the DNA-MMP solution was added to 100 μL of the diluted target DNA solution, and the mixture was incubated for 1 h at room temperature under shaking. Then, 20 μL of a TC-AuNC solution (10 pM) was added to the target- DNA-capturing MMP solution, and the mixture was incubated for 30 min at room temperature under shaking. During incubation (target-capturing step in **Figure 1.1**), sandwich hybridization complexes (NC-complex-**1**) were formed. The resulting NC-complex-**1** solution was washed three times with 0.3 M PBSS buffer, and the solution volume was adjusted to 10 μL. To form the AuNC clusters, 20 μL of the SA-AuNC solution (50 pM) was added to the prepared NC-complex-**1** solution, and the mixture was incubated further for 30 min at room temperature under shaking. During incubation (signal-amplifying step in **Figure 1.1**), the assembled AuNC cluster-MMP hybridization complexes (NC-complex-**2**) were formed. Finally, the NC-complex-**2** solution was washed three times with 0.3 M PBSS buffer and concentrated to a volume of 10 μL. To prepare

NS-complex-**2**, I followed the procedure above but replaced the TC- and SA-AuNCs with the TC- and SA-AuNSs.

Micro-Raman measurements for SERS-based DNA detection assay

For the Raman analysis, 5 μL of the prepared complex solutions was poured over a cover glass and concentrated using a magnet placed under the cover glass. The remaining solvent was removed by drying under ambient conditions. The dried cover glass was then inverted, and the focus was adjusted on the backside of the sample. All the Raman measurements were performed using a Renishaw inVia Raman microscopy system equipped with a 633 nm (190 μW) excitation laser, a standard charge-coupled device array detector (576 × 384 pixels; Peltier; cooled to −70 °C), and a 50× objective lens (NA = 0.75, Leica). The SERS spectra were obtained using an acquisition time of 10 s and were recorded for wavenumbers of 500–1,800 cm^{-1}.

Theoretical calculations of electric near-field

The BEM simulation was performed using the MNPBEM toolbox.[32-34] The edge length and radius of curvature at the corners of the AuNCs were taken to be 50 nm and 5 nm, respectively. The diameter of the AuNSs was 50 nm. The gap size between the AuNCs in the assembled AuNC clusters was estimated to be 2 nm, based on transmission electron microscopy (TEM) images (**Figure 1.3**). I regarded the surrounding environment to be air (n=1) and used Johnson and Christy's data for the dielectric function of gold.[35] The excitation wavelength was 633 nm.

Characterization

The morphologies of the synthesized nanoprobes and assembled AuNC clusters were evaluated using a TEM system (H-7600, Hitachi). The UV-vis spectra were obtained using a UV-vis spectrophotometer (HP 8453, Agilent Technologies). The fluorescence measurements for the quantification of the DNA-loading capacity were performed using a fluorophotometer (FP-8300, JASCO Inc.).

1.3. Results and Discussion

As the plasmonic nanoprobes for the SERS-based DNA detection assays, I first synthesized two types of nanoparticles (AuNCs and AuNSs) using the seed-mediated growth and surface-protection methods.[28,29] The synthesized AuNCs were further refined by depletion-induced flocculation in surfactant micelle solutions (for details, see the Supporting Information).[30] The synthesized AuNCs and AuNSs showed high uniformity in size and shape, exhibiting very high yields (>95%) (**Figure 1.4**a,b). In addition, the average sizes (edge length for the AuNCs and diameter for the AuNSs) of the products were similar, with both exhibiting narrow size distributions: 50.7 ± 0.6 nm for the AuNCs and 50.6 ± 0.7 nm for the AuNSs. The ultraviolet-visible (UV-vis) spectra of the AuNCs and AuNSs showed the sharp extinction peaks at 563 and 529 nm, respectively (**Figure 1.4**c). The optical properties (in particular, the extent of EM field enhancement for SERS) of plasmonic nanoparticles are highly dependent on their morphology.[36-38] Therefore, structural uniformity and a narrow size distribution would ensure that the variability in the SERS signal from the products is very low, making the products reliable and reproducible and thus highly suited for SERS-based DNA detection.

Subsequently, the surfaces of the AuNCs and AuNSs were functionalized with target-DNA-strand-capturing oligonucleotides (for details, see the Supporting Information). The DNA-modified plasmonic nanoparticles underwent sequence-specific hybridization during DNA detection (**Figure 1.4**d–g). During the target-capturing step (**Figure 1.1**), in the presence of complementary DNA strands (hepatitis A virus DNA; HAV

DNA), the assay solution, which was collected using a magnet, turned colorless, and the intensity of the extinction peak decreased sharply (**Figure 1.4**d). This confirmed that the TC-AuNCs were hybridized with the DNA-MMPs that captured the target DNA strands, forming a sandwich hybridization complex (NC-complex-**1** in **Figure 1.1**) (**Figure 1.4**e). However, when I replaced the target DNA with a non-complementary DNA strand (hepatitis B virus DNA; HBV DNA), the color of the solution as well as the extinction spectrum did not change, indicating that NC-complex-**1** had not been formed (**Figure 1.4**d,e). This DNA-sequence-specific hybridization process also occurred during the signal-amplifying step. When I added complementary SA-AuNCs that can be captured by DNA on NC-complex-**1** to a solution of NC-complex-**1**, the assay solution became transparent under an external magnetic field, and the intensity of the extinction peak decreased significantly in the supernatant solution because of the formation of the hybridized complexes (NC-complex-**2** in **Figure 1.1**) (**Figure 1.4**f,g). It should be noted that most assembled AuNCs were matched with each other in a face-to-face manner. On the other hand, in the case of non-complementary SA-AuNCs, the solution color and extinction spectrum did not change, indicating the high specificity of this assay (**Figure 1.4**f,g).

Next, I measured the DNA-loading capacity of the individual nanoparticles (the total amount of DNA attached on the surfaces of the nanoparticle). To quantify the DNA-loading capacity of a single nanoparticle, I dissolved the DNA-modified nanoparticles using potassium cyanide and measured the fluorescence signal of the fluorophore (Cy3)-

labeled DNA strands, released from nanoparticles. The total number of attached DNA strands on the surfaces of the individual nanoparticles was calculated from a standard curve obtained using the same DNA in known concentrations (**Figure 1.2**) (for details, see the Supporting Information). The DNA-loading capacity of a single AuNC (5004 ± 9 per particle) was much higher than that of a single AuNS (2934 ± 21 per particle) because of the larger surface area of the former, even though the two nanostructures had the same particle diameter. It should be noted that the DNA-loading densities (the number of attached DNA strands per the unit surface area of the nanoparticle) of the two types of nanoparticles were similar: 0.325 nm^{-2} for the AuNCs and 0.365 nm^{-2} for the AuNSs. Although the DNA-loading density of the AuNCs was similar to that of the AuNSs, the number of "effectively binding DNA strands" that could participate in hybridization was higher because of the flat structural feature-based straight-up binding between nearly all the untilted DNA strands at the interfaces of AuNCs (**Figure 1.5**a; facet junctions).[39] When spherical nanoparticles form assemblies, the number of the effectively binding DNA strands that are interacting with each other with correct orientations overlapping complementary sequences can be low owing to their convex surface structure (**Figure 1.5**a; point junctions) and heterogeneously tilted DNA strands at the interfaces of AuNSs.

Next, I investigated and compared the particle shape(particularly, curvature)-dependent binding kinetics of the various target-capturing nanoprobes (TC-probes; TC-AuNCs, and TC-AuNSs) during DNA hybridization (target-capturing step in **Figure 1.1**). During the DNA

hybridization process, I monitored the decrease in the extinction peak intensity of the assay solution (**Figure 1.6**), which was indicative of the consumption of the nanoprobes owing to the formation of the sandwich hybridization complexes (NC- or NS-complex-**1**) (for details, see the Experimental Section). The extinction intensity at a certain time (A_t) was divided by the initial intensity (A_0), and the relative extinction intensity (A_t/A_0) was plotted against the hybridization time (t). The plot of A_t/A_0 versus t could be fitted well using an exponential decay function: $A_t/A_0 = C \cdot \exp(-k \cdot t) + b$, where k is the decay constant. As shown in **Figure 1.5**b, the amount of the TC-probes consumed by the target-capturing MMPs during DNA hybridization was similar for the two constructs, resulting in them having similar decay constants ($k_{\text{TC-AuNC}} = 0.1203$ and $k_{\text{TC-AuNS}} = 0.1257$ min^{-1}) and half-lives ($t_{1/2}$; $t_{1/2,\ \text{TC-AuNC}} = 5.76$ and $t_{1/2,\ \text{TC-AuNS}} = 5.51$ min) (**Table 1.2**). This could be because, compared to nanoparticle surfaces, the MMPs contained a very large number of binding sites on their micron-sized surfaces, the probabilities of the TC-AuNCs and TC-AuNSs binding to the MMPs were similar, and the shape (curvature) effect with respect to DNA hybridization was probably negated because of the roughened surfaces of the MMPs (**Figure 1.4**e).

In contrast, the effect of the shape on the binding kinetics was obvious when signal-amplifying nanoprobes (SA-probes; SA-AuNCs and SA-AuNSs) were binding to complex-**1** (signal-amplifying step in **Figure 1.1**). The SA-AuNCs were consumed more rapidly by complex-**1** structures than were SA-AuNSs, indicating that the binding (hybridization) rate between the cubic nanoprobes (SA-AuNCs) was higher (**Figure 1.5**c). As a

result, the binding kinetics of the SA-AuNCs exhibited a higher decay constant and a shorter half-life ($k_{SA\text{-}AuNC}$ = 0.0428 min^{-1}, $t_{1/2,\ SA\text{-}AuNC}$ = 16.21 min) than did the kinetics of the SA-AuNSs ($k_{SA\text{-}AuNS}$ = 0.0367 min^{-1}, $t_{1/2,\ SA\text{-}AuNS}$ = 18.87 min) (**Table 1.2**). Further, the average decay rate up to $t_{1/2}$ (defined in terms of the moles of the nanoprobes consumed until the half-life per unit half-life) was estimated to be 7.54 and 4.35 attomoles·min^{-1} for the SA-AuNCs and SA-AuNSs, respectively. Interestingly, in contrast to the binding between the nanoprobes and the MMPs (target-capturing step in **Figure 1.1**), the cubic nanoprobes exhibited enhanced binding (hybridization) efficiency, with the binding rate being approximately 73% higher as compared to that of the spherical nanoprobes (signal-amplifying step in **Figure 1.1**). I believe that the presence of a higher number of the effectively binding DNA strands for the cube particles resulted in the faster binding rate. The enhanced binding (hybridization) kinetics, which were related to the shape (curvature) effect, would shorten the assay time and higher sensitivity of DNA hybridization for SERS-based DNA detection.

Next, I tested the hypothesis that the assembled nanoprobes would bind to each other more tightly and more uniformly if the number of the effectively binding DNA strands were high. To verify this hypothesis, I subjected the clusters to temperature-induced dissociation. In particular, to determine the strength of the structure-dependent binding between the nanoprobes precisely and to prevent any errors that may arise because of hybridization between the nanoprobes and the MMPs, I used AuNC or AuNS aggregates without MMPs. Once the nanoprobes had aggregated in solution, the interparticle distance decreased to less than the average particle

size, resulting in a concomitant change in the solution color and the UV-vis spectrum (**Figure 1.7**).[40] As the solution temperature was increased, the nanoprobe aggregates were dissociated above the melting temperature (T_m) of DNA. Here, I monitored the change in the intensity of the extinction peak of the dissociating nanoprobes as the temperature of the solution increased from 25 to 85 °C. The AuNC aggregates showed a higher T_m (74.8 °C) compared to that of the AuNS aggregates (71.2 °C) (**Figure 1.5**d). Further, the dissociation for the AuNC aggregates was steeper and sharper than that for the AuNS aggregates (**Figure 1.5**d), and the full width at half maximum (FWHM) values obtained from the first-order derivatives of the dissociation curves were estimated to be 2.8 and 4.0 °C for the AuNC and AuNS aggregates, respectively (inset, **Figure 1.5**d). In general, the aggregates formed by the DNA-modified Au nanoparticles exhibited a much higher T_m as well as a much sharper melting transition (i.e., narrow FWHM) than those of the aggregates formed by the free duplex DNA with the same DNA sequence owing to the greater cooperative effect in the former.[41,42] This cooperative effect on the melting transition of DNA has been investigated both experimentally and theoretically and is highly dependent on conditions such as the surface DNA density, DNA sequence, salt concentration, interparticle distance.[42,43] In this study, I showed the nanoparticle-structure-dependent melting transition of DNA, and the difference in the surface morphologies of the nanoparticles induces a difference in the number of effective DNA binders as well as the binding strength and uniformity in DNA hybridization. Thus, the presence of a small number of the effectively binding DNA strands leads to the dissociation process occurring relatively

quickly and heterogeneity in DNA binding on particle surface, resulting in a change in the UV-vis spectrum at low temperatures as well as a broad transition temperature range. On the other hand, the presence of a large number of the effective DNA binders allows the aggregates to remain intact at relatively high temperatures, with the UV-vis spectrum changing very sharply because the aggregates dissociate simultaneously near the complete dissociation point of the effective DNA binders due to homogenous and uniform binding/dissociation environment of the effectively binding DNA strands. Analogously, the dissociation of the AuNS clusters occurred relatively earlier, at a lower temperature (lower T_m), and over a relatively broad transition range (broader FWHM) because of the lack of the effective DNA binders between the AuNSs and the heterogenous environment of DNA. Contrastingly, the presence of a higher number of the homogenously modified effective DNA binders in the case of the AuNC aggregates helped them maintain their structure even at a higher temperature (higher T_m), with the dissociation of the nanoprobes occurring over a very narrow range of transition temperatures (narrower FWHM). This effect causes the assembled clusters to be formed faster and more efficiently, and the assembled structures can last longer and more stably, thereby inhibiting the uncontrollable loss of the SERS signal during the assay processes or measurements. Additionally, I monitored the changes in the intensity of the extinction peak of the DNA-modified nanoprobes as the temperature of the solution was decreased from 85 to 25 °C (**Figure 1.8**). The DNA-modified AuNC nanoprobes started to be hybridized at higher solution temperature (77.0 °C) compared to the DNA-modified AuNS nanoprobes (73.0 °C).

Further, the AuNC nanoprobes formed aggregates more rapidly; the FWHM values obtained from the first-order derivatives of the hybridization (aggregation) curve were estimated to be 10.5 and 12.4 °C for the AuNC and AuNS nanoprobes, respectively (inset, **Figure 1.8**). These experimental results further indicate that a higher number of the effective DNA binders on nanoparticles caused by the shape (curvature) effect lead to faster, stronger and more uniform binding between DNA-modified nanoprobes.

Finally, I performed the hierarchic-nanocube-assembly-based ultrasensitive DNA detection assay using the SERS technique. To detect the target DNA (HAV), I performed a sandwich-hybridization assay using the DNA-MMPs and TC-AuNCs, which resulted in the formation of NC-complex-**1**. To enhance the intensity of the SERS signal from NC-complex-**1**, I introduced SA-AuNCs into NC-complex-**1** to form three dimensionally (3D) assembled plasmonic AuNC clusters on the MMPs (NC-complex-**2**). **Figure 1.9**a,b show the changes in the SERS signal intensity of the NC-complexes as a function of the target DNA (HAV) concentration. The sequence-specific hybridization ability of the proposed system (**Figure 1.4**d–g) means that, during a control experiment with non-complementary HBV DNA, the intensity of the SERS signal from NC-complex-**1** and NC-complex-**2** was negligibly low (the blue and green dots in **Figure 1.9**a; the blue and green spectra in **Figure 1.9**b). In the case of NC-complex-**1**, the SERS signal intensity (the black dots in **Figure 1.9**a; the black spectra in **Figure 1.9**b) was distinguishable, in contrast to the case of the control experiment; however, the limit of detection (LOD) was only ~1 pM. Significantly, the SERS signal intensity of the assembled plasmonic AuNC

clusters (NC-complex-**2**) was highly enhanced, and the LOD was largely improved to ~100 aM (the red dots in **Figure 1.9**a; the red spectra in **Figure 1.9**b). The strong plasmonic coupling at the assembled area of the AuNC clusters resulted in a 10000-fold improvement in the sensitivity for DNA detection. Next, the SERS-based DNA detection results with the differently shaped nanoparticles were compared (**Figure 1.9**c). In case of the assembled plasmonic clusters formed by the AuNSs (NS-complex-**2**), the SERS signal intensity was lower than that for NC-complex-**2** — the LOD was limited to approximately 10 fM. Furthermore, in comparison to NC-complex-**2**, NS-complex-**2** exhibited greater variations in its detection signal intensity (i.e., higher standard deviations) during repetitive measurements, which was indicative of relatively poorer reproducibility and reliability with respect to DNA detection — the standard deviations obtained from five independent samples were 8.3–15.6% and 18.2–38.6% for the NC- and NS-complex-**2**, respectively. The facet-to-facet coupling that occurred between the AuNC-based clusters, which resulted in homogenous and uniform plasmonic coupling over a wide region of the assembled area, the point-to-point coupling between the AuNS-based clusters resulted in an unstable, non-uniform, and less reproducible SERS signals. From these results, I concluded that AuNCs are the optimal structure for SERS-based analytical applications requiring sensitive, reproducible, and reliable results.

To verify that a strong and uniform electric field was generated within the gap region of the AuNC clusters, I performed boundary element method (BEM) simulation using the MNPBEM toolbox (**Figure 1.10**).[32-34] During the BEM simulations, when a linearly polarized light (wavelength

633 nm) was illuminated on a single AuNC, a weak electric field was generated only at the corner of the AuNC because of the absence of plasmonic coupling (**Figure 1.10**a). In contrast, a markedly stronger electric field was generated within the gap region of the AuNC clusters because of strong plasmonic coupling (**Figure 1.10**b). In particular, the strong electric field was spread across a large area of the assembled AuNC clusters, owing to facet-to-facet coupling. This phenomenon is quite different from that observed in the case of the AuNS clusters, which generated an electric field only at a highly localized small spot (point-to-point coupling) because of their convex surface morphology (**Figure 1.10**c). Furthermore, unlike the AuNS clusters amplifying the electric field only at a specific gap region with a plasmonic coupling direction parallel to the incident light, the AuNC clusters strongly amplified the electric field over a wide area of the assembled planes for all different coupling directions within the cluster (**Figure 1.10**d–i). Due to the planar metal/insulator/metal geometry, AuNC assembly carries the transverse gap plasmon (TGP),[44,45] which is a propagating surface plasmon along metal/gap/metal interfaces. Under the illumination, the TGPs are excited at the faces normal to the incident polarization. Reaching edges, excited TGPs can propagate to adjacent faces, which are parallel to the incident polarization. Therefore, unlike AuNS assembly, enhanced electric field spans every nanogap in AuNC assembly and gives much larger probability of Raman molecules being inside hot spot, resulting in strongly and uniformly enhanced electric field. Considering that the hierarchically assembled clusters are randomly formed in various orientations on the surface of the spherical magnetic

microparticles, the cubic-plasmonic-nanoparticle-based clusters, which amplify the electric field uniformly and strongly on all assembled surfaces regardless of the direction of incident light, provide a more uniform, reproducible and quantitative signals for SERS-based DNA detection than spherical-plasmonic-nanoparticle-based clusters.

1.4. Conclusions

I developed a hierarchic-nanocube-assembly-based SERS assay for DNA detection with high sensitivity and target specificity in a stable, reproducible, reliable, and quantitative manner. Due to the uniform and strong plasmonic coupling between AuNCs, the assembled AuNC clusters exhibited significantly higher sensitivity (higher by a factor of 10000) than non-assembled AuNCs, with the LOD improving to approximately 100 aM without optimization. The AuNCs with flat surfaces, which had a higher number of the effectively binding DNA strands, exhibited a higher binding rate, higher melting temperature, and sharp melting transition during DNA hybridization as compared to those of widely used spherical nanoparticles, suggesting that the shape (curvature) effect further enhances the binding efficiency, strength, and stability of the assembled clusters. The results show that uniformly formed nanocubes are promising building blocks for chemical/biological ligand-based materials assembly and quantitative plasmonics, and the proposed H-Cube-SERS method opens new avenues for the design and application of highly SERS-active nanostructures for use in ultrasensitive and quantitatively reproducible biosensing platforms.[3,45-47]

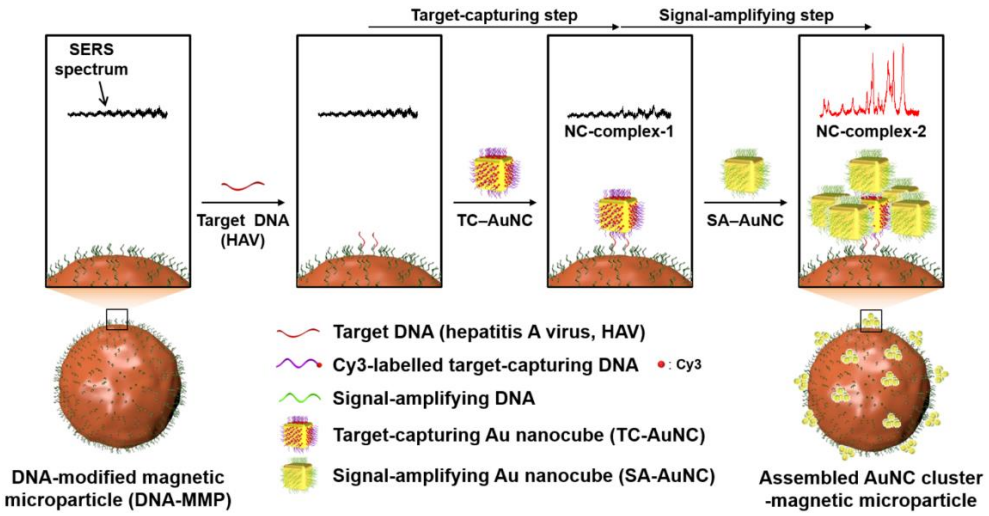

Figure 1.1. Schematic illustration of hierarchic-nanocube-assembly-based SERS (H-Cube-SERS) assay for DNA detection.

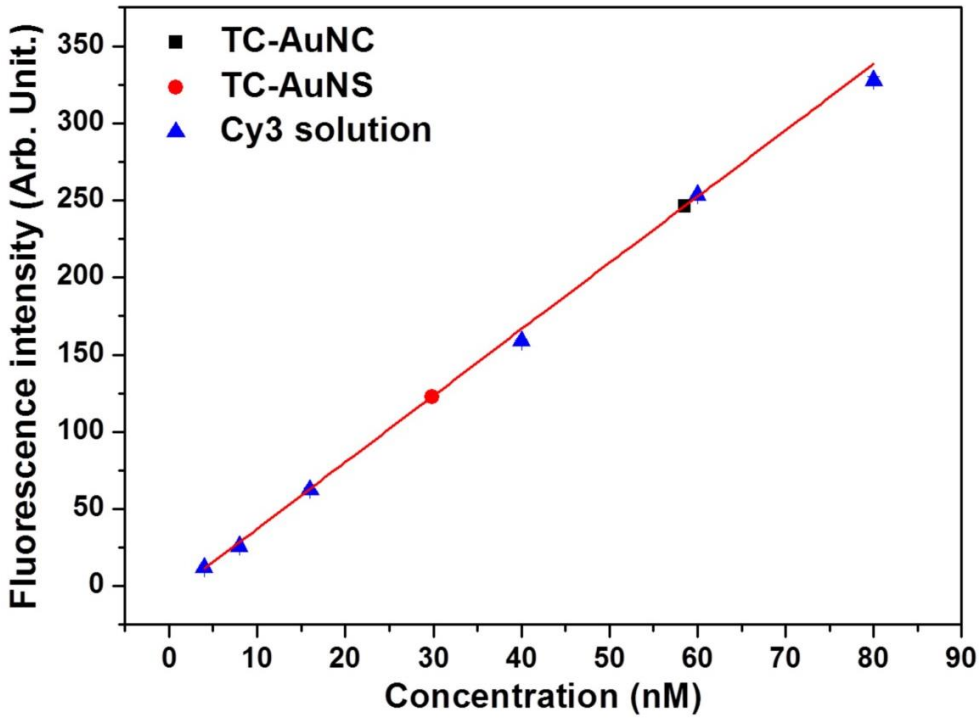

Figure 1.2. Standard curve (red line) of fluorescence (Cy3) signal intensity for known concentrations of Cy3-labeled DNA strands (blue dots) for quantification of DNA-loading capacity of 50-nm-sized AuNCs and AuNSs. Fluorescence signal intensities of DNA detached from AuNCs (black dot) and AuNSs (red dot) are indicated on the standard curve.

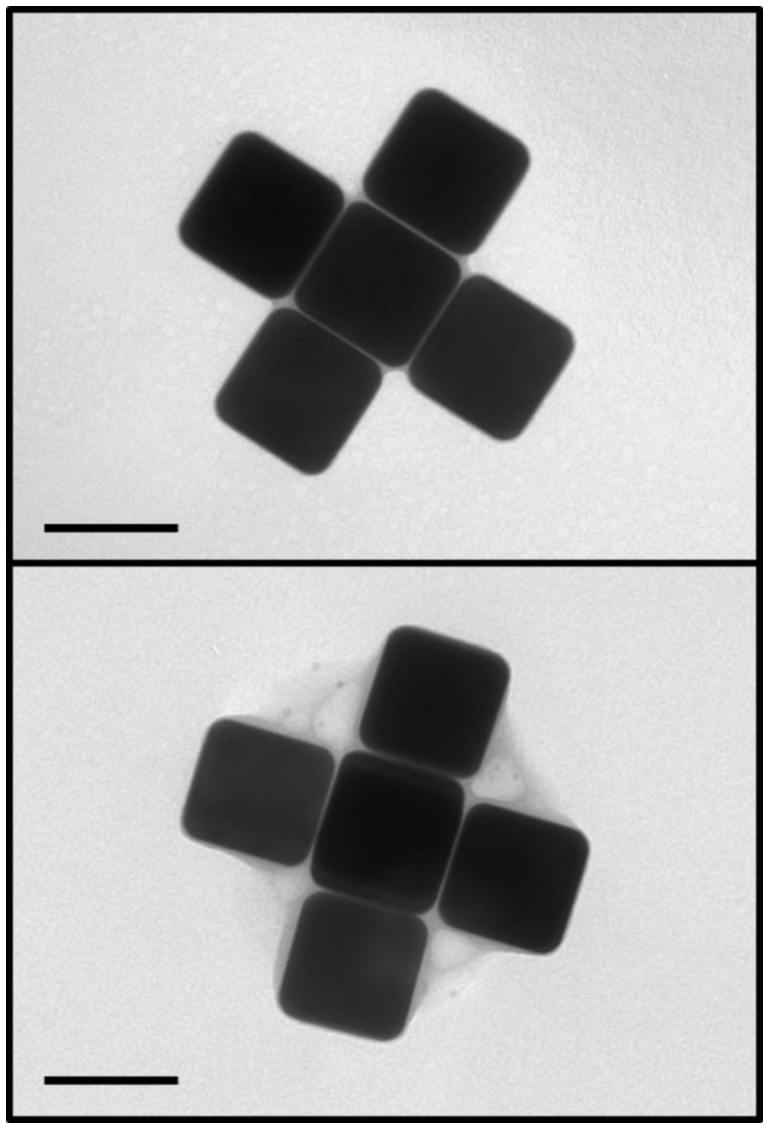

Figure 1.3. TEM images of assembled AuNC clusters via hybridization between TC- and SA-AuNCs. Scale bars are 50 nm.

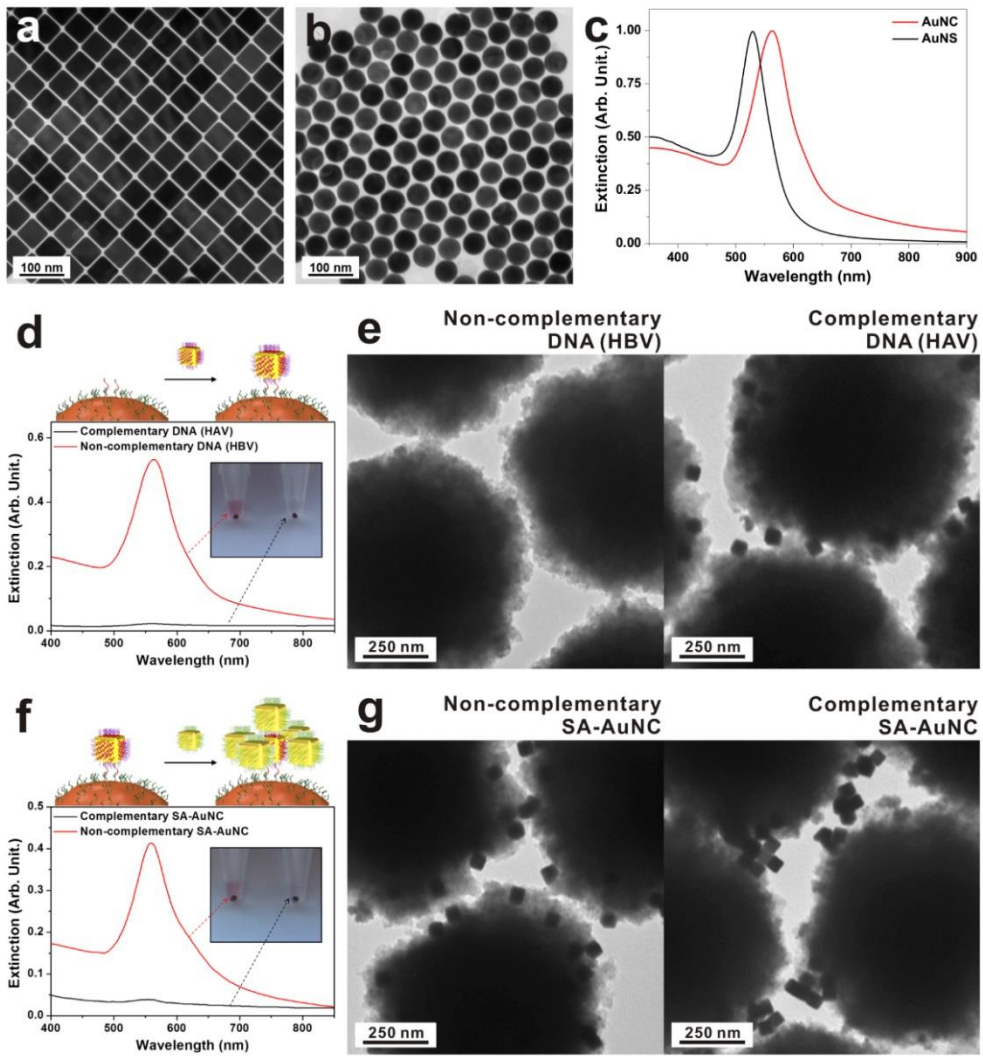

Figure 1.4. Synthesis of AuNCs and AuNSs and characterization of DNA-sequence-specific hybridization properties of assembled Au nanocube clusters. (a,b) TEM images of synthesized nanoparticles: (a) AuNCs and (b) AuNSs. (c) UV-vis spectra of synthesized nanoparticles. (d–g) DNA-sequence-specific hybridization ability for selective capturing of (d,e) target DNA strands and (f,g) SA-AuNCs. (d,f) Changes in UV-vis spectrum of assay solution collected using external magnetic field after (d) target-capturing step and (f) signal-amplifying step. Inset: Color of assay solution

under magnetic field after DNA hybridization. (e,g) TEM images of sequence-specific sandwich hybridization complexes formed (e) by different linker DNAs during target-capturing step and (g) by different SA-AuNCs during signal-amplifying step.

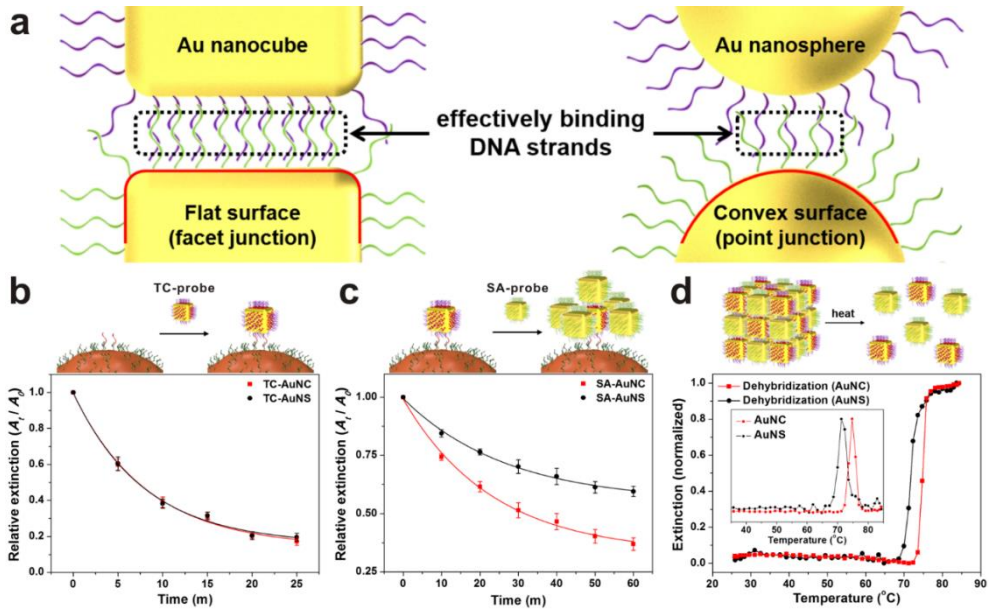

Figure 1.5. Shape (curvature) effect-induced binding of DNA-modified nanoparticles and their dissociation properties. (a) Schematic illustration of shape (curvature) effect for hybridization between DNA-modified Au nanoparticles. Owing to structural features, in case of AuNCs (flat surface), number of DNA strands that participate in DNA hybridization (termed "effectively binding DNA strands") is higher than that in case of AuNSs (convex surface), suggesting that a shape (curvature) effect occurs. Number of the effectively binding DNA strands present influences binding and dissociation properties of DNA-modified nanoparticles; higher number of the effectively binding DNA strands would result in faster binding rate and higher melting transition temperature. (b,c) Structure-dependent DNA binding kinetics during (b) target-capturing step and (c) signal-amplifying step denoted in Figure 1. (d) Structure-dependent dissociation of nanoprobe aggregates. Inset: First-order derivatives of dissociation curve of AuNC and AuNS aggregates.

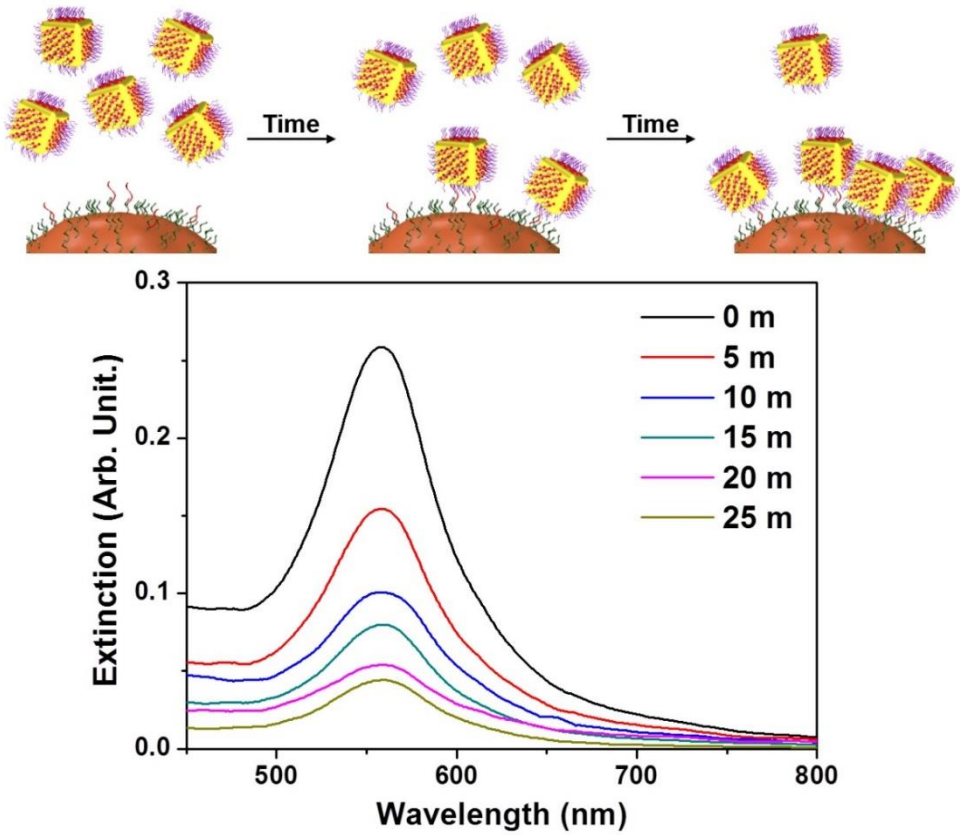

Figure 1.6. UV-vis spectra of assay solution as function of hybridization time.

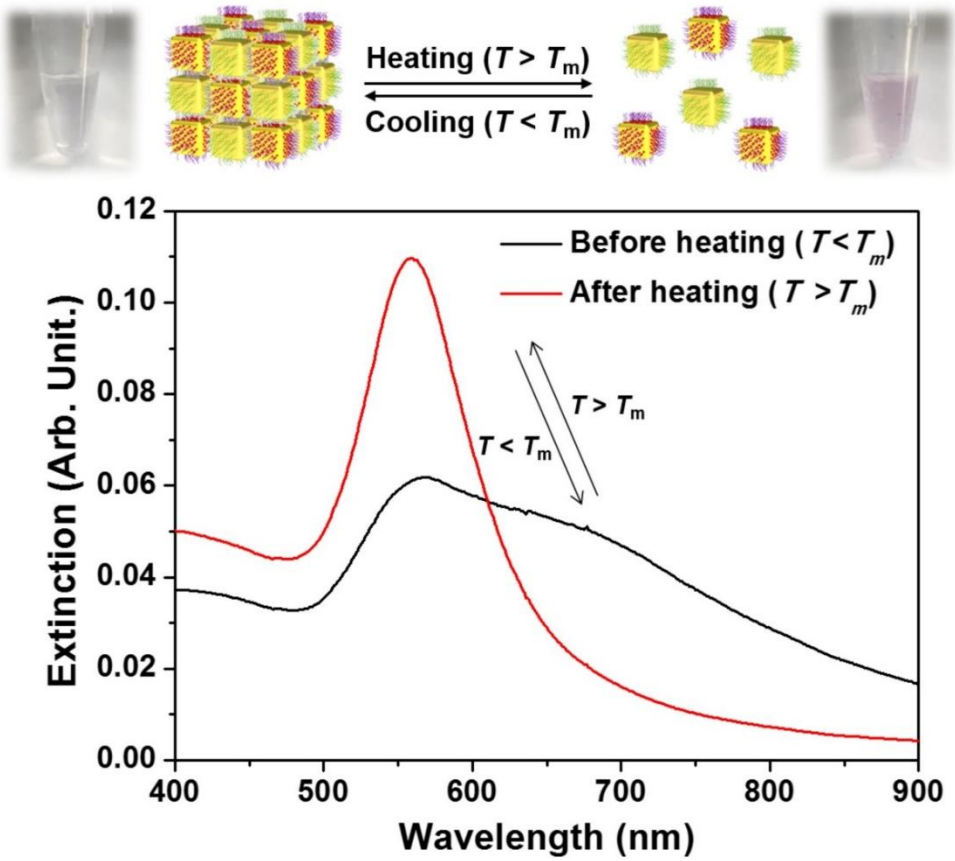

Figure 1.7. Changes in UV-vis spectra and solution color of aggregated AuNC with solution temperature.

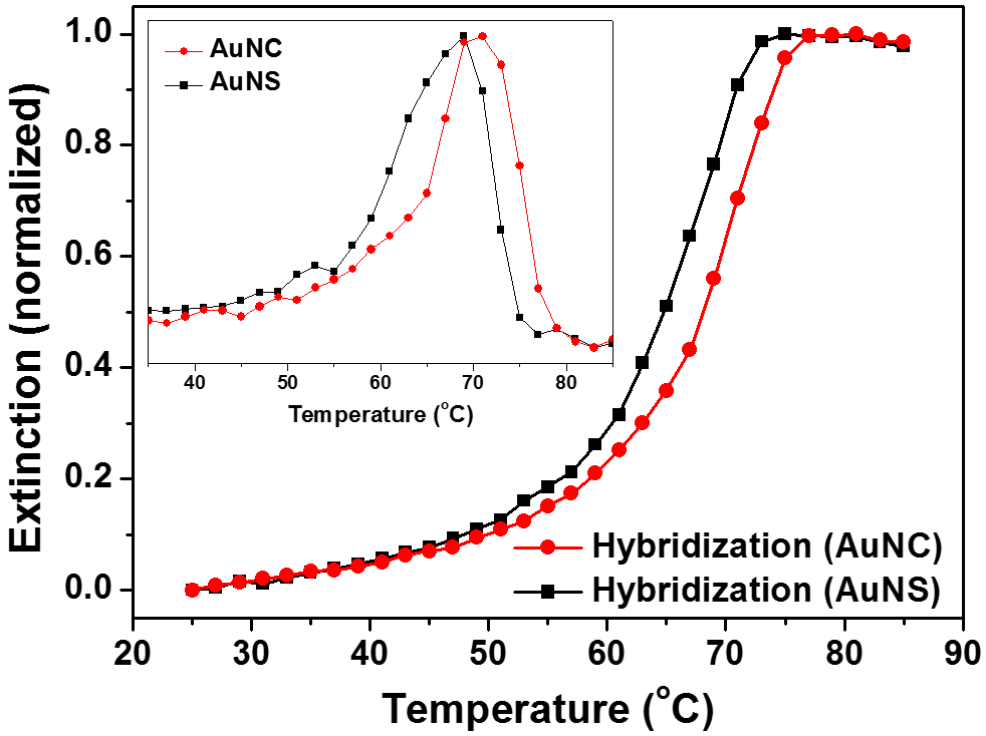

Figure 1.8. Structure-dependent hybridization curve of DNA-modified nanoprobes. Intensity of extinction peak of DNA-modified nanoprobes were monitored as solution temperature was decreased from 85 to 25 °C. Due to the shape (curvature) effect, DNA-modified AuNC nanoprobes started to be hybridized at higher solution temperature and formed aggregates more rapidly (i.e., narrow FWHM) compared to DNA-modified AuNS nanoprobes. Inset: First-order derivatives of hybridization (aggregation) curve of DNA-modified AuNC and AuNS nanoprobes.

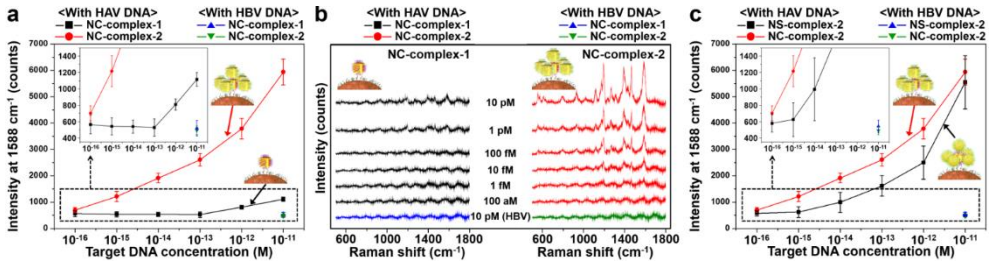

Figure 1.9. SERS-based ultrasensitive DNA detection using 3D assembled plasmonic nanoprobe clusters. (a) Plot of SERS signal intensities of AuNC-MMP complexes (NC-complex-**1** and NC-complex-**2**) for different concentrations of target DNA (HAV, 100 aM–10 pM) and non-complementary target DNA (HBV, 10 pM). (b) SERS spectra of AuNC-MMP complexes (NC-complex-**1** and NC-complex-**2**) for different concentrations of DNA strands. (c) Plot of SERS signal intensities of AuNC- and AuNS-MMP complexes (NC-complex-**2** and NS-complex-**2**) for different concentrations of target DNA (HAV, 100 aM–10 pM) and non-complementary target DNA (HBV, 10 pM). All spectra were acquired using 633-nm (190 μW) excitation laser and acquisition time of 10 s and were recorded for wavenumbers of 500–1,800 cm^{-1}.

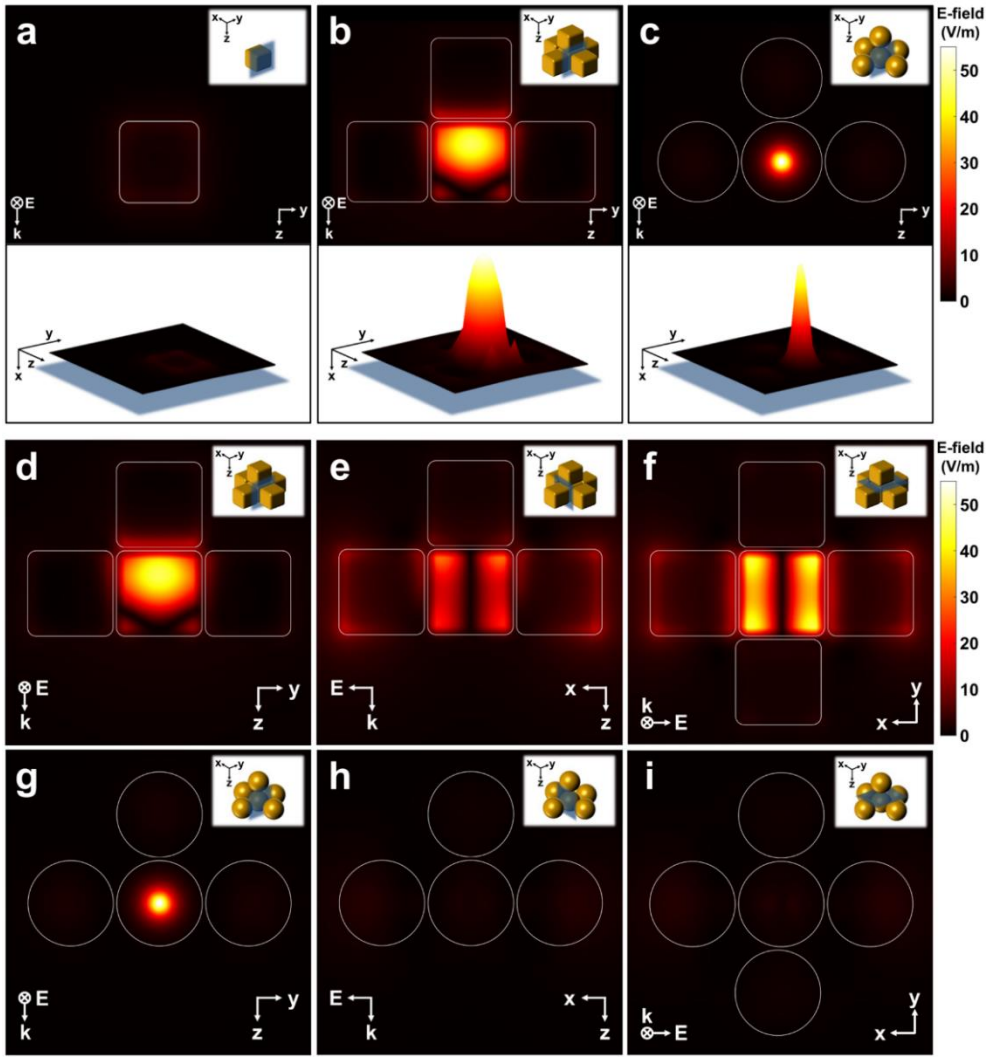

Figure 1.10. Boundary element method (BEM) simulation of electric near-field of single plasmonic nanoparticle and 3D assembled nanoparticle clusters. (a–c) 2D (upper panel) and 3D (lower panel) plot of electric near-field distribution of (a) single AuNC, (b) 3D assembled AuNC cluster, and (c) 3D assembled AuNS cluster. Insets: 3D structural models used for BEM simulation. Blue-shaded region indicate planes (*y*-*z* planes) at which electric fields were evaluated. (d–i) 2D plot of electric near-field distribution of 3D assembled clusters formed by (d–f) AuNC and (g–i) AuNS. Blue-shaded region indicate planes at which electric fields were evaluated: (d,g) *y*-*z*

planes, (e,h) *x*-*z* planes, and (f,i) *x*-*y* planes. For all cases, a linearly polarized light in *x*-direction (wavelength 633 nm) was illuminated in the *z*-direction.

Table 1.1. DNA sequences used in this work.

DNA	Sequence (5' to 3')
Target-capturing DNA for MMPs	NH_2-A_{10}-PEG_6-AGAAAGAGGAGTTAA
Cy3-labeled target-capturing DNA for TC-probes	TCCATGCAACTCTAA-A_{10}-**Cy3**-SH
Signal-amplifying DNA for complementary SA-probes	TTAGAGTTGCATGGA-A_{10}-SH
Signal-amplifying DNA for non-complementary SA-probes	TAACAATAATCCCTC-A_{10}-SH
Hepatitis A virus (HAV)	TTAGAGTTGCATGGATTAACTCCTCTTTCT
Hepatitis B virus (HBV)	TTGGCTTTCAGTTATATGGATGATGTGGTA

Table 1.2. Summary of the binding kinetics results of the TC-probes and SA-probes.

		Decay constant (k, min^{-1})	**Half-life ($t_{1/2}$, min)**	**Average decay rate until $t_{1/2}$† ($R_{half\text{-}life}$, amole/min)**
TC-probes	TC-AuNCs	0.1203 ± 0.0110	5.76 ± 0.53	13.51 ± 1.26
	TC-AuNSs	0.1257 ± 0.0130	5.51 ± 0.58	13.79 ± 1.47
SA-probes	SA-AuNCs	0.0428 ± 0.0038	16.21 ± 1.45	7.54 ± 0.68
	SA-AuNSs	0.0367 ± 0.0036	18.87 ± 1.88	4.35 ± 0.44

†The $\boldsymbol{R}_{half\text{-}life}$ defined in terms of the moles of the nanoprobes consumed until the half-life per unit half-life.

Chapter 2

Plasmonically Enhanced Catalytic Properties of Ag/Pt Composite Nanostructures for SERS Signal-Based Real-Time Monitoring of Catalytic Chemical Reaction

2.1. Introduction

Platinum (Pt) has been intensively exploited in fields of catalysis due to surface-sensitive chemical properties enabling a strong coupling with a chemisorbed hydrogen (or oxygen or any oxygen-containing species) on its surface.[46,47] In case of Pt, anti-bonding states between the hydrogen 1s and metal d-band are empty; therefore, coupling between the adsorbates and Pt surface give rise to attractive interaction rather than repulsive force.[46] This strong binding caused by intrinsic local electronic structure can dissociate the reactants efficiently for utilizing in catalytic reactions; this is critical reason why the Pt exhibits excellent performance in catalytic reaction. However, the utilization of Pt as catalyst generally experiences critical limitation in the practical use due to its high cost and scarcity.[48] In addition, it generally suffers from sluggish kinetics and surface poisoning causing insufficient catalytic activity and selectivity, because of strongly adsorbed intermediate species.[49-51]

Recently, metal alloy nanocatalysts (i.e., combining two or more different metals within single structure) have been considered as a promising alternative for overcoming the limitations of when using monometallic Pt in catalysts.[52-56] When Pt is alloyed with other transition metals (e.g., iron, cobalt, nickel, etc.) the geometric (e.g., surface morphology, surface-lattice strain, crystal structures) and electronic (d-band center shift) structures of the Pt are systemically modified due to the atomic rearrangement and strain at the metal alloy surface.[46,57,58]

Eventually, the adsorption strength between the reactants/intermediates and the Pt-based alloy metal surface can be modulated positively (i.e., weakened

binding) in terms of catalytic activity and selectivity, which leads to reducing the surface poisoning during catalytic reaction and enhancing the catalytic performance compared to the monometallic Pt catalysts.[46,47,59,60]

When Pt forms alloyed nanostructure with other noble-metals, such as gold (Au), silver (Ag), copper (Cu), a synergistic effect on the catalytic activity, especially in the photocatalysis, can be expected by achieving both superior catalytic (from Pt) and optical/plasmonic (from noble-metals) merits simultaneously in single alloyed nanoparticle. When light is irradiated onto the noble-metal nanostructures, free electrons on the surface of nanoparticles collectively oscillate at the same frequency as external light, producing a localized surface plasmon (LSP).[61-63] While the highly excited and energetic LSPs decay, light can be re-emitted or highly energetic hot-hole pairs are generated through radiative and non-radiative decay processes, respectively.[61,64] Importantly, the photoexcited energetic electrons, called as 'hot electrons', exhibit several effects on the photochemistry, photoemission, photodesorption, photocurrent, electrical doping, and local heating,[62,64] giving versatile feasibility for the development of photodetection, photovoltaics, and photocatalysts.[65-67] Especially in the case of photocatalysts, the photoexcited hot electrons can be transferred to the adjacent reactants located near the surface of plasmonic noble-metal nanoparticles, which eventually allows to trigger and promote a plasmon-driven photocatalytic chemical reaction.[61] Up to now, many studies have shown that such a hot electron generation and injection process under light illumination can efficiently improve the catalytic activity in the various field, such as photo-reduction, hydrogen dissociation, organic reaction, water-

splitting, degradation of organic compounds, etc.[68-72] So far, various researches have been proved the existence of hot electrons and their role in catalytic chemical reaction, and have been also intensively accomplished that the photocatalytic reaction can be efficiently promoted with the improving catalytic performance by hot electrons generated by the plasmonic noble-metals;[70,71] however, the kinetic and quantitative analysis of how much can hot electrons contribute to boost the rate of catalytic chemical reactions has been rarely conducted, yet.

Here, I present bimetallic alloyed nanostructures consisting of plasmonically photoactive moiety (Ag) and catalytic moiety (Pt) for a surface-enhanced Raman scattering (SERS) signal-based real-time monitoring of catalytic chemical reaction under laser irradiation (**Figure 2.1**). The plasmonically (Ag) and catalytically (Pt) active bi-functional nanostructure is synthesized through galvanic replacement reaction between cuboidal Ag nanoshell structure (cuboidal AgNS) and Pt ions. From this bimetallic alloyed nanostructure, the partially doped Pt on the surface of Ag nanostructure serves catalytically active sites in the presence of $NaBH_4$ promoting chemical conversion from 4-nitrothiophenol (4-NTP) to 4-aminothiophenol (4-ATP), while Ag nanostructure under excitation laser irradiation produces strongly enhanced electromagnetic field near the nanoparticle surface and generates highly energetic hot electrons. Due to the plasmonic properties of Ag component that exhibit the strong SERS intensity, the changes of SERS spectra of reactant (4-NTP) and product (4-ATP) can be efficiently monitored during catalytic chemical reaction in real-time. Importantly, the Ag component can generate the highly energetic hot

electrons by its superior plasmonic feature, which thereby promotes the catalytic chemical reaction more efficiently and provides improvement of conversion rate constant even with a small amount of Pt content in the bimetallic Ag/Pt nanoparticles. The results of the improvement of the conversion rate constant by hot electron generation and transfer process under light illumination pave the pathways to designing the bi-functional alloyed metallic nanostructures for the development of highly efficient photocatalysts.

2.2. Experimental Section

Reagents and materials

Gold(III) chloride trihydrate ($HAuCl_4 \cdot 3H_2O$), silver nitrate ($AgNO_3$), cetyltrimethylammonium bromide (CTAB), L-ascorbic acid (AA), 4-nitrothiophenol (4-NTP), 4-aminothiophenol (4-ATP), 2-naphthalenethiol (2-NT), 4-nitrophenol (4-NP), and ethyl alcohol were purchased from Sigma-Aldrich. Potassium tetrachloroplatinate(II) (K_2PtCl_4) and sodium borohydride ($NaBH_4$) were purchased from Alfa Aesar. Cetyltrimethylammonium chloride (CTAC) was purchased from Tokyo Chemical Industry Co., Ltd. All the chemical reagents were used as received without further purification. In all experiments, NANOpure water (Millipore Milli-Q, 18.2 MQ·cm) was used.

Synthesis of Au nanorods (AuNRs)

The AuNRs were synthesized using the seed-mediated growth method by following previous literature.[73] To synthesize CTAB-capped Au seeds, firstly, aqueous solutions of $HAuCl_4 \cdot 3H_2O$ (0.5 mM, 5 mL) and CTAB (200 mM, 5 mL) were mixed in a 50-mL round bottom flask at 27 °C under magnetic stirring (500 rpm). After one min, a freshly prepared ice-cold $NaBH_4$ aqueous solution (10 mM, 0.6 mL) was quickly injected into the flask, and the reaction mixture was stirred 2 min at 500 rpm. The brown-colored CTAB-capped Au seeds were further incubated at 27 °C for 4 h without agitation. For the seed-mediated growth of AuNRs, aqueous solutions of $HAuCl_4 \cdot 3H_2O$ (1 mM, 10 mL) and CTAB (200 mM, 10 mL) were mixed, then aqueous solutions of $AgNO_3$ (4 mM, 0.6 mL), AA (78.8

mM, 140 μL), and CTAB-capped Au seeds (24 μL) were sequentially added to the mixture with gentle shaking. The reaction mixture was further incubated overnight at 30 °C without agitation. Finally, the resulting solution was washed twice with distilled water by centrifugation at 12,000 rpm for 10 min and redispersed in distilled water for further use.

Synthesis of cuboidal Ag nanoshell structures (cuboidal AgNSs)

The cuboidal AgNSs were synthesized by following previous literature with a modification.[74] Briefly, a solution of as-prepared AuNRs (300 pM, 10 mL) was mixed with a CTAC aqueous solution (15 mM, 10 mL) in a 100-mL round bottom flask, and the solution was allowed to heat until 60 °C under magnetic stirring (500 rpm). To form cuboidal Ag shells onto AuNRs, aqueous solutions of $AgNO_3$ (1.5 mM, 10 mL) and AA (10 mM, 10 mL) were sequentially added to the mixture. The reaction solution was stirred for 10 s, then allowed to growth at 60 °C for 4 h without agitation. Finally, the resulting solution was washed with distilled water by centrifugation at 8,000 rpm for 10 min and redispersed in distilled water for further use.

Synthesis of bimetallic Ag/Pt nanoparticles (Ag/Pt NPs)

Ag/Pt NPs were prepared by utilizing a conventional galvanic replacement reaction.[75,76] Firstly, a solution of as-prepared cuboidal AgNS (100 pM, 3 mL) and a CTAC aqueous solution (5 mM, 7 mL) were added to a 25-mL vial and heated to 80 °C under magnetic stirring (500 rpm). To incorporate Pt ions on the Ag shell, appropriate volume (50, 100, and 150 μL) of aqueous K_2PtCl_4 solution (50 μM) was added to the above mixture using a

syringe pump (Legato 110, KD Scientific) at a rate of 10 $mL \cdot h^{-1}$. After all volume of the K_2PtCl_4 solution was added to the reaction mixture, the resulting solution was further heated for 10 min until the solution became stable. Finally, the resulting solution was cooled to room temperature, then washed twice with distilled water by centrifugation at 8,000 rpm for 10 min and redispersed in distilled water for further use.

Surface modification of bimetallic Ag/Pt nanoparticles

Ethanolic solutions of 4-NTP (5 mM, 5 μL) and 2-NT (2.5 mM, 5 μL) were simultaneously added to as-synthesized nanocatalysts (Ag/Pt NPs; 100 pM, 1 mL) and the mixture solution was gently shaken at room temperature for 2 h. Unbound 4-NTP and 2-NT were removed by centrifugation at 8,000 rpm for 10 min, then the precipitates was redispersed in distilled water to be nanocatalysts' concentration of 200 pM. In the case of surface modification with a single component, each ethanolic solution of 4-NTP, 4-ATP, or 2-NT (5 mM, 5 μL) was added separately to the nanocatalysts (100 pM, 1 mL), and the rest of the procedure was same as case for the surface modification with 4-NTP and 2-NT.

***In situ* monitoring of catalytic reaction using Raman spectra**

For the investigation of hot-electron-mediated catalytic activity of the as-synthesized nanocatalysts, the time-dependent spectral changes in Raman spectra for transformation from 4-NTP to 4-ATP were monitored under laser irradiation. Typically, a freshly prepared $NaBH_4$ solution (200 mM, 50 μL) was injected to as-synthesized nanocatalysts (200 pM, 50 μL) of which

surface is decorated with 4-NTP and 2-NT, then reaction solution was quickly transferred to the Raman measurement stage. For the real-time monitoring of catalytical chemical reaction from the time-dependent changes in Raman spectra, all Raman spectra were acquired using 785 nm excitation laser at laser power density of 6.6×10^4 W/cm^2 (or different power density of 2.2×10^5 W/cm^2 and 4.2×10^5 W/cm^2) and acquisition time of 2 s at every measurements with interval of 1 s between each measurements.

***In situ* monitoring of catalytic reaction using UV–Vis spectra**

To evaluate the hot-electron-mediation-free catalytic activity of the as-synthesized nanocatalysts, the reduction of 4-nitrophenol (4-NP) to 4-aminophenol (4-AP) by $NaBH_4$ on nanocatalysts was adopted as a model reaction. Typically, a aqueous solution of 4-NP (0.4 mM, 0.75 mL) was mixed with 1 mL of distilled water in a quartz cuvette, and a freshly prepared $NaBH_4$ solution (480 mM, 0.25 mL) was quickly added. Finally, the nanocatalysts (10 pM, 0.5 mL) without 4-NTP and 2-NT on their surface was rapidly added into reaction solution. Thereafter, the decrease of the UV–Vis extinction intensity at λ = 400 nm, indicating the reduction of 4-NP to 4-AP, was continuously monitored as a function of time using UV–Vis spectrophotometer. To monitor the time-dependent changes in UV–Vis spectra, each UV–Vis spectrum was recorded in every 10 s, and the ratio of extinction intensity at each reaction time point (A_t) relative to its initial value (A_0) was used for calculating the conversion rate constant (k) under pseudo-first-order kinetics. For accuracy, the extinction intensity of the

nanocatalysts obtained in the solution without 4-NP was subtracted to correct all the extinction intensities obtained during the measurements.

Characterization

The morphological characteristics of the as-synthesized nanoparticles (e.g., AuNRs, cuboidal AgNSs, and Ag/Pt NPs) were investigated using a transmission electron microscopy (TEM) system (JEM-2100, JEOL) and a high-resolution TEM (HR-TEM) system (JEM-2100F, JEOL). Energy-dispersive X-ray spectroscopy (EDX) system (INCA, Oxford Instruments) coupled with a HR-TEM system was used for the elemental maps of the as-synthesized nanoparticles. The atomic ratio of metals in the nanoparticles was obtained with an inductively coupled plasma mass spectrometry (ICP-MS) analysis. The UV–Vis spectra were obtained with an UV–Vis spectrophotometer (HP 8453, Agilent Technologies). All the Raman measurements were performed using a Renishaw inVia microscope equipped with 785 nm excitation laser, a standard charge-coupled device (CCD) array detector (576 × 384 pixels; Peltier; cooled to -70 °C), and a 20× objective lens (NA = 0.40, Leica).

2.3. Results and Discussion

Gold nanorods (AuNRs) were synthesized through a seed-mediated growth by following previous literature,[73] and which allow us serve as a core material for manufacturing cuboidal Ag nanoshell structures (cuboidal AgNSs) (**Figure 2.1**).[74] Next, I fabricated the bimetallic Ag/Pt nanoparticles (Ag/Pt NPs) by employing Pt ions to the cuboidal AgNSs. Through the chemical reaction (i.e., galvanic replacement reaction)[75] between Pt ions ($PtCl_4^{2-}$) and Ag atoms (Ag^0), the Pt ions are partially deposited on the surface of cuboidal AgNSs, resulting in formation of bimetallic Ag/Pt nanoparticles. Especially, in here, I controlled the degree of galvanic replacement reaction by adjusting the added amount of Pt ions, resulting that I obtained Ag/Pt NPs with different Ag/Pt atomic ratio (**Figure 2.3**). When a small amount of Pt ions (50 μL) was employed to the cuboidal AgNSs, the structural changes of bimetallic nanostructure (i.e., Ag/Pt NP-50) were not significantly observed with the transmission electron microscopy (TEM) image (**Figure 2.3**a) compared to the cuboidal AgNSs (**Figure 2.2**); however, it was confirmed that a small amount of Pt was doped on the surface of the Ag nanostructures through the EDX mapping (**Figure 2.3**d). With further increasing the added amount of Pt ions (100 and 150 μL) during galvanic replacement reaction (i.e., Ag/Pt NP-100 and Ag/Pt NP-150), the surface of Ag nanostructures was more roughened and the formation of small holes on the surface of Ag nanostructures were clearly observed (**Figure 2.3**b,c), caused by the relatively high degree of galvanic replacement reaction between Pt^{2+} and Ag^0. In addition, the EDX mapping of these bimetallic nanostructures indicate that the higher amount of Pt was

doped on the surface of the Ag nanostructures (Figure 2e,f). As a result, the Ag and Pt atomic ratio within each bimetallic nanoparticles obtained through an inductively coupled plasma mass spectrometry (ICP-MS) analysis was $Ag_{99.3}$-$Pt_{0.7}$, $Ag_{98.3}$-$Pt_{1.7}$, and $Ag_{97.6}$-$Pt_{2.4}$ for Ag/Pt NP-50, Ag/Pt NP-100, and Ag/Pt NP-150, respectively. In addition, the ultraviolet–visible (UV–Vis) spectra of the synthesized bimetallic nanoparticles changed according to the amount of Pt loading. For the cuboidal AgNSs without Pt loading, the four LSPR peaks (346, 405, 457, and 560 nm) were clearly seen in the UV–Vis spectrum due to their structural features of anisotropic geometry with both corner and edge (**Figure 2.2**).[74] For the case of Ag/Pt NPs, however, the LSPR peaks were slightly broadened and shifted, and the extinction intensities were decreased as increasing the amount of Pt loading (**Figure 2.4**). Those spectral changes of Ag/Pt NPs indicate that the atomic ratio within bimetallic nanostructures were quantitatively tuned according to the degree of the galvanic replacement reaction (i.e., smaller amount of Ag when larger amount of Pt), which results in the changes of plasmonic properties.

It should be note that the generation of hot electrons are closely related to the plasmonic activity of plasmonic nanoparticles.[77] In order to investigate and compare the plasmonic (i.e., SERS) activity of as-synthesized Ag/Pt NPs depending on the substituted amount of Pt in the cuboidal AgNSs, I measured SERS spectra of Raman molecules decorated onto the surface of nanoparticles (**Figure 2.5**). When the cuboidal Ag shell was formed onto AuNRs, Raman signal intensity was highly enhanced compared to AuNRs, due to the intrinsic fact that Ag is generally superior to

Au in terms of plasmonic property. However, when Pt was introduced on the surface of the cuboidal AgNSs (i.e., Ag atoms are substituted with Pt atoms), the Ag/Pt NPs exhibited lower Raman signal intensities than a cuboidal AgNS regardless of the amount of Pt introduced into the cuboidal AgNSs (**Figure 2.5** and **2.6**). More importantly, the Raman signal intensity gradually decreased as the substituted amount of Pt increased, which is because the proportion of Ag contributing to the strong SERS activity is reduced (**Figure 2.6**). For this reason, the SERS activity of Ag/Pt NPs was decreased compared to the cuboidal AgNSs, however, it still generated strong Raman signal intensity compared to that of AuNRs and is sufficient for real-time monitoring of chemical reaction using Raman spectra.

Together with the analysis of excellent plasmonic properties of bimetallic Ag/Pt nanoparticles, which are mainly caused by Ag components, I next investigated their catalytic properties facilitated by Pt components present on Ag/Pt NPs. Notably, I mainly focused on the effect of hot electrons on improving the conversion rate of catalytic chemical reactions and examined the synergistic effects that can be expected from bimetallic nanostructure consisting of plasmonic (Ag) and catalytic (Pt) metals, under laser irradiation. As a catalytic chemical reaction model, I adopted the well-known reduction reaction where the nitro group in the reactants chemically attached to the surface of metallic nanocatalysts are transformed to amino group in the presence of sodium borohydride ($NaBH_4$).[78,79] First of all, I confirmed the catalytic capability of as-synthesized nanocatalysts for the chemical reaction model by observing the chemical conversion from 4-NTP to 4-ATP through changes in the Raman spectra. Before adding $NaBH_4$,

which drives the catalytic chemical reaction through metal hydrides produced by the reaction between borohydride ions and metal surfaces,[80,81] to the Ag/Pt bimetallic nanocatalyst with 4-NTP on the particle surface, the typical Raman peaks corresponding to 4-NTP (332, 530, 724, and 855 cm^{-1}) were clearly observed (**Figure 2.7**). Ten minutes after adding $NaBH_4$, however, those Raman peaks disappeared completely and the typical Raman peaks corresponding to 4-ATP (392 and 640 cm^{-1}) were newly observed, which indicates chemical conversion from 4-NTP to 4-ATP without forming other by-products. This catalytic feature was observed in all cases of Ag/Pt NPs regardless of the amount of Pt loading (**Figure 2.7**). In addition, in case of Ag/Pt NPs with 2-NT molecules that have no functional groups related to the chemical reduction reaction, no spectral change in typical Raman peaks corresponding to 2-NT (368, 519, 599, 639, 767, and 845 cm^{-1}) was observed even with the addition of $NaBH_4$ (**Figure 2.8**). These results clearly show that the proposed chemical reduction reaction occurs completely and selectively on the Ag/Pt bimetallic nanocatalysts.

In order to evaluate the contribution of hot electrons in enhancing the efficiency of catalytic chemical reactions (specifically, reaction kinetics), I monitored the changes in the Raman spectra of reactant (4-NTP) functionalized on the plasmonic nanoparticles in real-time. Firstly, I prepared a solution of Ag/Pt NPs with both 4-NTP and 2-NT on their surface. After adding $NaBH_4$ to the nanocatalysts solution, the changes in the Raman spectra during chemical reaction were recorded at every 2 seconds (see details in Supporting Information). **Figure 2.9** clearly shows that, as the chemical reaction proceeds, the typical Raman peaks

corresponding to 4-NTP gradually disappears (orange-colored dashed line) and those corresponding to 4-ATP simultaneously appears (blue-colored dashed line). Please note that I used typical Raman peak of 2-NT (599 cm^{-1}), which is independent to chemical reaction, as an internal standard (green-colored dashed line) for more accurate quantitative analysis in evaluating reaction kinetics. Since a large excess amount of $NaBH_4$ is used here, it can be assumed that the chemical conversion from 4-NTP to 4-ATP follows pseudo-first-order kinetics.[82] Thus, the conversion rate constant (***k***) was determined by following Equation (1):

$$\boldsymbol{kt} = -\mathbf{ln}\left(\frac{[\mathbf{4\text{-}NTP}]_t}{[\mathbf{4\text{-}NTP}]_{t=0}}\right) = \mathbf{ln}\left(\frac{(I_{724}/I_{599})_t}{(I_{724}/I_{599})_{t=0}}\right) \qquad \text{Equation (1)}$$

where, $[4\text{-NTP}]_t$ is the concentration of 4-NTP at different measurement time points (***t***) during chemical reaction, and I_{724} and I_{599} are the typical Raman signal intensities of 4-NTP (at 724 cm^{-1}, assigned to the C–S stretching vibration) and 2-NT (at 599 cm^{-1}, assigned to the ring deformation band), respectively.[81,83,84] From above equation, I plotted the logarithm of the relative Raman signal intensity (i.e., I_{724}/I_{599}) recorded at the beginning (***t***=0) and at certain measurement points (***t***) in the chemical reaction to calculate the conversion rate constant (***k***).

Figure 2.10 shows the experimental results of real-time monitoring of catalytic chemical reactions measured from as-synthesized nanocatalysts with different amounts of Pt loading. In the case of cuboidal AgNSs not containing Pt (**Figure 2.10**a), the chemical reaction was not initiated even for a long time after the addition of $NaBH_4$ and catalytic conversion

proceeded very slowly (i.e., gentle slope, indicating a low ***k*** value), which is due to the relatively lack of catalytically active sites that initiate and boost the metal hydrides-mediated reduction reaction: $\boldsymbol{k}_{\text{cuboidal AgNS}} = 3.660 \times 10^{-3} \pm 5.062 \times 10^{-4}\ s^{-1}$. In the case of Ag/Pt NPs, however, the chemical conversion (i.e. transformation from 4-NTP to 4-ATP) occurred immediately and proceeded very rapidly (i.e., steep slopes, indicating a high ***k*** value) compared to the cuboidal AgNSs without Pt loading: $\boldsymbol{k}_{\text{Ag/Pt NP-50}} = 2.696 \times 10^{-2} \pm 1.663 \times 10^{-3}\ s^{-1}$, $\boldsymbol{k}_{\text{Ag/Pt NP-100}} = 2.117 \times 10^{-2} \pm 1.027 \times 10^{-3}\ s^{-1}$, $\boldsymbol{k}_{\text{Ag/Pt NP-150}} = 1.860 \times 10^{-2} \pm 1.063 \times 10^{-3}\ s^{-1}$ (**Figure 2.10**b–d). When the temperature of the solution was measured during the catalytic reaction (**Figure 2.11**), an increase (or change) in the reaction solution temperature was hardly observed regardless of the kind of the as-synthesized nanocatalyst, due to very low concentrations of nanoctalysts (100 pM) — Although the reaction temperature generally rises by about 1 °C, the difference in reaction temperature according to the kind of the nanocatalyst is only less than about 0.3 °C. These results indicate that changes in solution temperature under laser irradiation have a minor effect on the difference of the conversion rate constant, in our case.

Surprisingly, Ag/Pt NPs with the lowest loading of Pt exhibited the fastest conversion rate (Ag/Pt NP-50; **Figure 2.10**e,f), which is opposed to the fact that the catalytic reaction rate constant generally increases in proportion to the amount of catalyst (Pt in our case). Unlike the conventional catalytic reaction models not involving light, in this study, the catalytic chemical reaction was evaluated by monitoring the changes in Raman spectra of reactants (4-NTP) under laser irradiation. In particular, the

Ag/Pt NPs synthesized in this study simultaneously contain Pt that robustly initiates and promotes catalytic reaction and Ag that exhibits excellent plasmonic properties, within a single nanostructure. In this case, this unusual tendency in the catalytic properties is expected to be due to the possibility that the hot electrons generated by the plasmonic behavior of Ag under laser irradiation are partly involved in the chemical reaction. In other words, for the case of Ag/Pt NPs with a low loading of Pt (Ag/Pt NP-50), the nanocatalysts exhibits excellent plasmonic properties because of the relatively large amounts of Ag remaining within nanoparticles, which leads to robust generation of hot electrons. This suggests that energetic hot electrons contribute significantly to the overall catalytic chemical reaction as an additional electron source, and consequently improve the conversion rate of the chemical reaction even with very low loadings of Pt that mainly responsible for catalytic properties.

In order to verify these assumptions, I further investigated the changes in chemical conversion rate constant depending on the power density of irradiated laser. The plasmonic properties of metallic nanoparticles are highly related to the power density of irradiated laser, which indicates that under intense laser irradiation, more hot electrons can be generated and practically involved in the chemical reaction. In these respects, the higher power of the irradiated laser, the faster the chemical conversion rate (**Figure 2.12**a–c), which demonstrates that the plasmon-driven generation and transfer of hot electrons substantially contributes to the efficiency of the catalytic chemical reaction: $2.696 \times 10^{-2} \pm 1.663 \times 10^{-3}$ s^{-1}, $3.886 \times 10^{-2} \pm 1.200 \times 10^{-3}$ s^{-1}, and $4.262 \times 10^{-2} \pm 2.820 \times 10^{-3}$ s^{-1} for the

power density of irradiated laser of 6.6×10^4 W/cm^2, 2.2×10^5 W/cm^2, and 4.2×10^5 W/cm^2, respectively. To more intuitively analyze the generation of hot electrons of Ag/Pt NPs that vary with the power density of irradiated laser, I observed the chemical transformation from 4-NTP to *p,p*'-dimercaptoazobenzene (DMAB) with spectral changes in the representative Raman peaks of each molecule: 1080, 1110, and 1347 cm^{-1} for 4-NTP; 1140, 1390, and 1436 cm^{-1} for DMAB (**Figure 2.12**d). The conversion of 4-NTP, which introduced on the surface of plasmonic nanostructures, to DMAB under the laser irradiation is a well-known and typical model showing feasibility of hot electrons for driving chemical reactions.[77,85,86] As expected, in the case of Ag/Pt NP-50 with strong laser power (4.2×10^5 W/cm^2), the ratio of Raman peak intensity of 4-NTP to that of DMAB (I_{1140}/I_{1080}) was larger than the cases with moderate and weak laser power (2.2×10^5 W/cm^2 and 6.6×10^4 W/cm^2): 0.101, 0.413, and 0.582 for the power density of irradiated laser of 6.6×10^4 W/cm^2, 2.2×10^5 W/cm^2, and 4.2×10^5 W/cm^2, respectively (**Figure 2.12**d). Thus, due to the critical contribution of Ag with superior plasmonic properties (i.e., SERS activities), it can be concluded that the bimetallic Ag/Pt nanoparticles with a relatively large amount of Ag can produce hot electrons more strongly. In here, it should be noted that these hot electrons generated strongly from the plasmonic nanoparticles will serve as additional electron sources capable of participating in the chemical reduction reaction, which eventually will contribute to enhance the efficiency of the overall catalytic chemical reaction (specifically, reaction kinetics). Given these experimental results (**Figure 2.10** and **2.12**), I believe that the unusual catalytic aspects of the

Ag/Pt NPs associated with the improvement of chemical reaction rates are caused by the direct transfer of hot electrons generated by plasmonic metals to the adjacent reactants.

Next, the conversion kinetics of the analogous chemical reaction — the reduction of 4-nitrophenol (4-NP) to 4-aminophenol (4-AP) in the presence of $NaBH_4$ — were additionally investigated by using as-synthesized nanocatalysts without 4-NTP and 2-NT on their surface. This catalytic reaction model has been adopted frequently to evaluate the catalytic properties because it allows simple, fast, and real-time monitoring of chemical reactions using UV–Vis spectrometers.[87,88] Here, I recorded the changes in UV–Vis spectra of reactant (i.e., 4-NP) over reaction time and observed the chemical conversion from 4-NP to 4-AP by monitoring the decreases of extinction intensity at λ = 400 nm (see details in Supporting Information) (**Figure 2.13**). Similar with Equation (1), the conversion rate constant (***k***) was calculated from the slope obtained by plot between the logarithm of relative extinction intensity at λ = 400 nm and the reaction time (***t***):

$$\boldsymbol{kt = -\ln(A_t/A_0)} \qquad \text{Equation (2)}$$

where, A_0 and A_t are the extinction intensities at λ = 400 nm recorded at beginning and at certain measurement time points after the addition of $NaBH_4$, respectively. In **Figure 2.14**, the catalytic reaction rate constants increased in proportion to the amount of Pt loaded within bimetallic nanocatalysts in this catalytic reaction model, which is consistent with a

general trend for the change of reaction rate with the amount of catalyst — the higher the amount of catalyst, the faster the reaction rate. Interestingly, this is obviously contrary to the tendency of reaction rate constant obtained under laser irradiation (**Figure 2.10**), which is expected to be due to the following reasons: 1) Because the irradiation intensity of UV–Vis light used for the monitoring of chemical conversion reaction (i.e., transformation from 4-NP to 4-AP) is very weak compared to that of the laser used for Raman spectra-based monitoring, hot electrons would not have been generated sufficiently to contribute significantly to the improvement of chemical conversion rate. Or, 2) Since the physisorbed reactants (i.e., 4-NPs) are allowed to spend a short time at the catalytically active sites during the chemical reaction and are detached from the metal surface immediately after the reaction is terminated, the transfer of hot electrons would not have been occurred enough to participate in the chemical reaction. On the other hand, in the previous cases where the catalytic chemical reaction was monitored through the changes in the Raman spectra, a high-power laser was used and the reactants (i.e., 4-NTP) were chemically attached directly onto the surface of metal catalysts; it is thus considered that the chemical conversion rate was improved due to the robust generation of hot electrons and their efficient transfer to adjacent reactants. These experimental results further support the reason for the unusual tendency of catalytic properties (specifically, reaction kinetics) occurred in the case of plasmonic nanocatalysts under the laser irradiation (**Figure 2.10** and **2.12**).

Recently, edgeless Ag–Pt bimetallic nanocages with hollow interiors have been demonstrated that the formation of undesired peroxide

intermediates could be suppressed by the plasmon-induced effect during electrochemical oxygen reduction reactions.[76] For the Ag–Pt bimetallic nanocatalysts system under light illumination, the transfer of plasmon-induced hot electrons could lead to higher electron population in antibonding of O_2 adsorbates bound on the surface of Pt atoms and weaken the O–O bond, which eventually facilitates the cleavage of weakened O–O bond and forms the desired H_2O products. On the contrary, in the absence of light illumination, the oxygen reduction reactions proceed favorably for the cleavage of O–Pt bond instead of O–O bond owing to the absence of the generation and transfer of hot electrons, which thereby leads to a formation of undesired peroxide ions (HO_2^-) and reduces the H_2O yield.[76] Analogously, the improvement of chemical reaction rates shown in our case might also be caused by the efficient transfer of plasmon-induced hot electrons, which highly reveals synergistic effects between the plasmonic Ag metals and the catalytic Pt metals distributed adjacent onto a single nanostructure surface. Furthermore, it could be expected that the electromagnetic field strongly enhanced by plasmonic nanostructure could promote the rapid migration or effective adsorption/desorption of reactants and products on the surface of nanocatalysts.[76] In our case, however, it is considered that the molecular behavior of the reactants and products caused by the aforementioned electromagnetic field enhancement might not significantly affect to the improvement of chemical reactions rates, because the reactants (4-NTP) and products (4-ATP) are chemically attached onto the surface of the nanocatalysts.

2.4. Conclusions

I report the bimetallic nanoparticle consisting of plasmonically photoactive Ag and catalytic Pt (Ag/Pt NP) for SERS-signal-based real-time monitoring of catalytic chemical reaction. The Ag/Pt NP was synthesized through conventional galvanic replacement reaction with Pt ions by using cuboidal Ag nanoshell structure (cuboidal AgNS) as a sacrificial template. The atomic ratio of Ag/Pt are adjusted by controlling the degree of galvanic replacement reaction. The synthesized Ag/Pt NPs showed excellent performance for the catalytic chemical reaction under laser irradiation regardless of the amount of Pt loading. Especially, the conversion rate constant of Ag/Pt NPs showed unusual tendency – the less Pt loading, the faster chemical reaction. It is considered that those unusual aspects might be caused by that the hot electrons generated by the plasmonic nanostructures under laser irradiation are transferred to the adjacent reactants onto the nanocatalysts and partly involved in the chemical reaction as an electron source; which consequently promote catalytic chemical reaction more rapidly (i.e., improvement of the conversion rate constant) even with very low loadings of catalytic Pt. The results of bimetallic nanostructures for the improvement of catalytic chemical reaction open avenues in designing of more efficient plasmonic nanocatalysts and facile hot-electron-engineering for efficient photocatalysts.

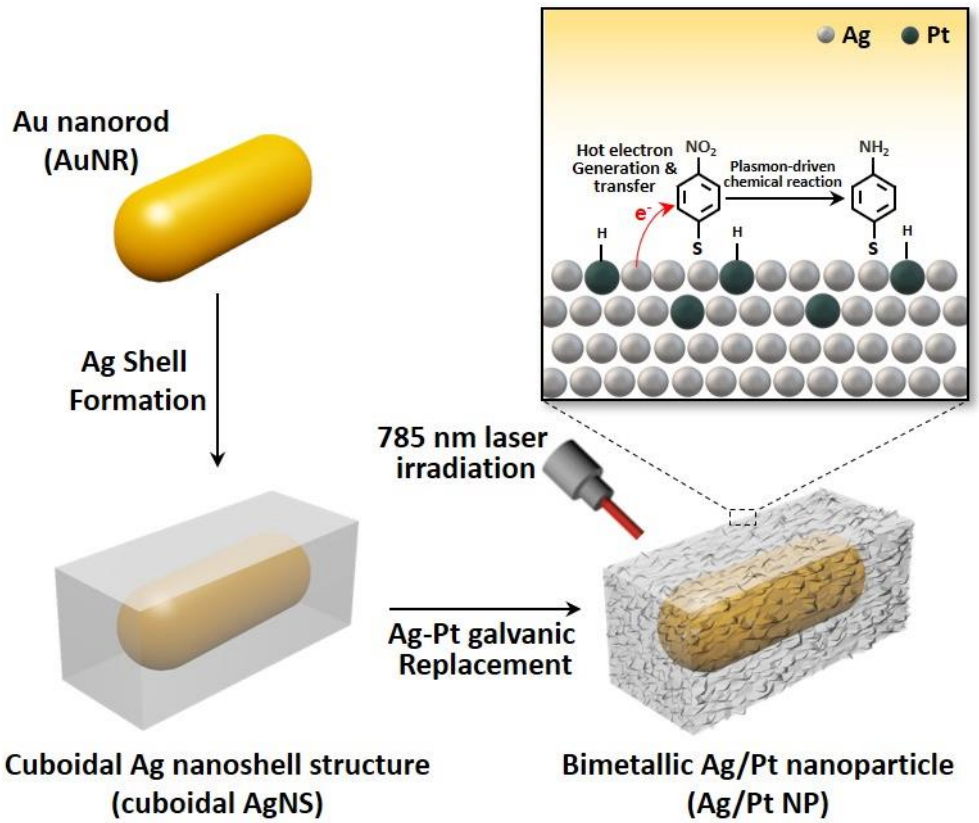

Figure 2.1. Schematic illustration of the plasmon-driven chemical reaction occurred on the surface of bimetallic Ag/Pt nanoparticle. From the bimetallic composite nanostructure, Pt partially doped on the surface of Ag nanostructure serves catalytically active sites in the presence of $NaBH_4$, while Ag nanostructure under excitation laser irradiation produces strongly enhanced electromagnetic field near the particle surface and generates highly energetic hot electrons. Especially, the former allows us strong intensity of Raman spectra enough to monitor the catalytic chemical reaction in real-time; and the latter conducts the generation/transfer of hot electron to the adjacent reactants bound onto the surface of nanostructure, resulting in improvement of catalytic conversion rate constant.

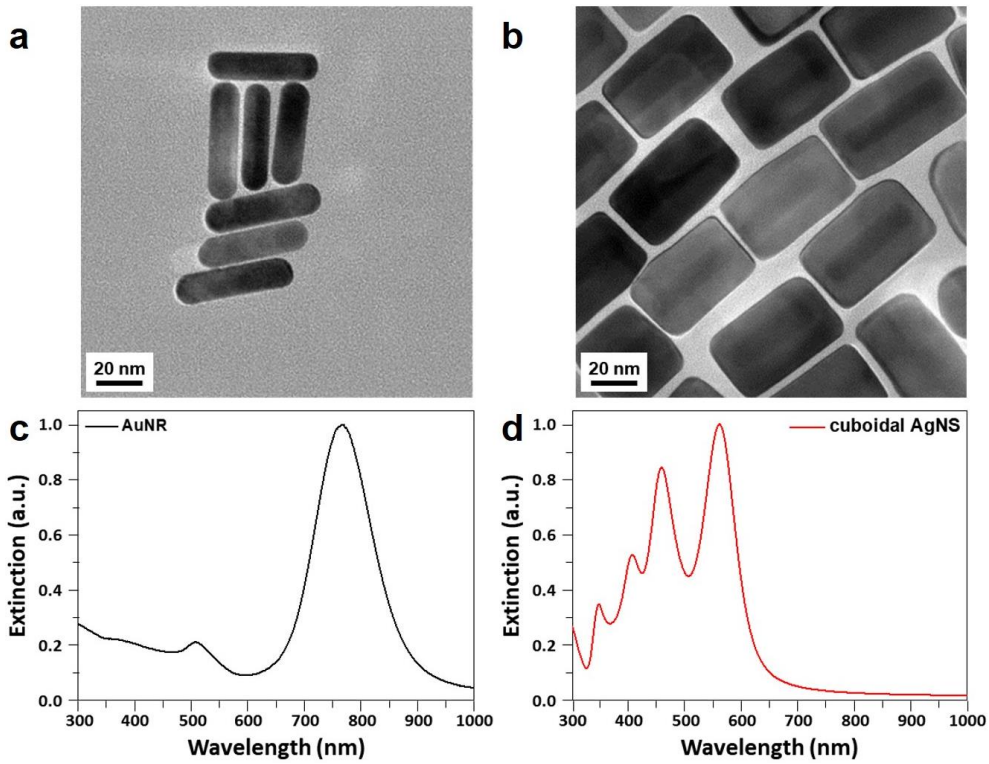

Figure 2.2. Transmission electron microscopy (TEM) images and system UV–Vis spectra of as-synthesized AuNR (a and c) and cuboidal AgNS (b and d).

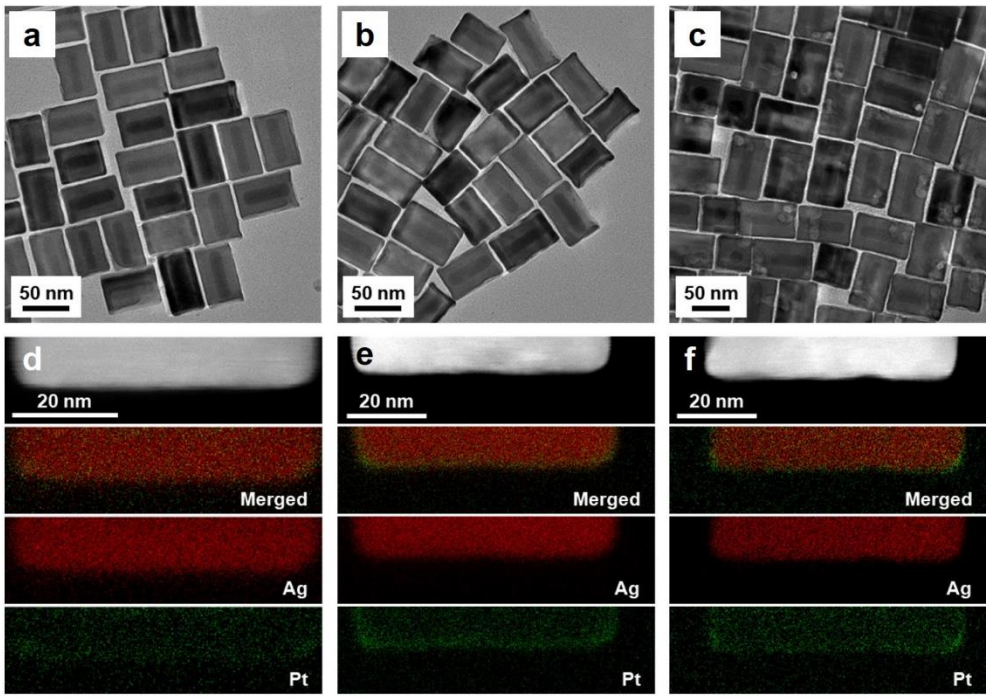

Figure 2.3. TEM images and EDX elemental mapping at the surface of as-synthesized bimetallic Ag/Pt NPs with different Ag/Pt atomic ratio: (a,d) Ag/Pt NP-50, (b,e) Ag/Pt NP-100, and (c,f) Ag/Pt NP-150. As the added amount of Pt ions during galvanic replacement reaction, the surface of nanoparticles are more roughened and the small holes are observed on the surface of nanoparticles, which indicates that more Pt atoms are doped (i.e., replaced) within the cuboidal Ag nanostructure surface.

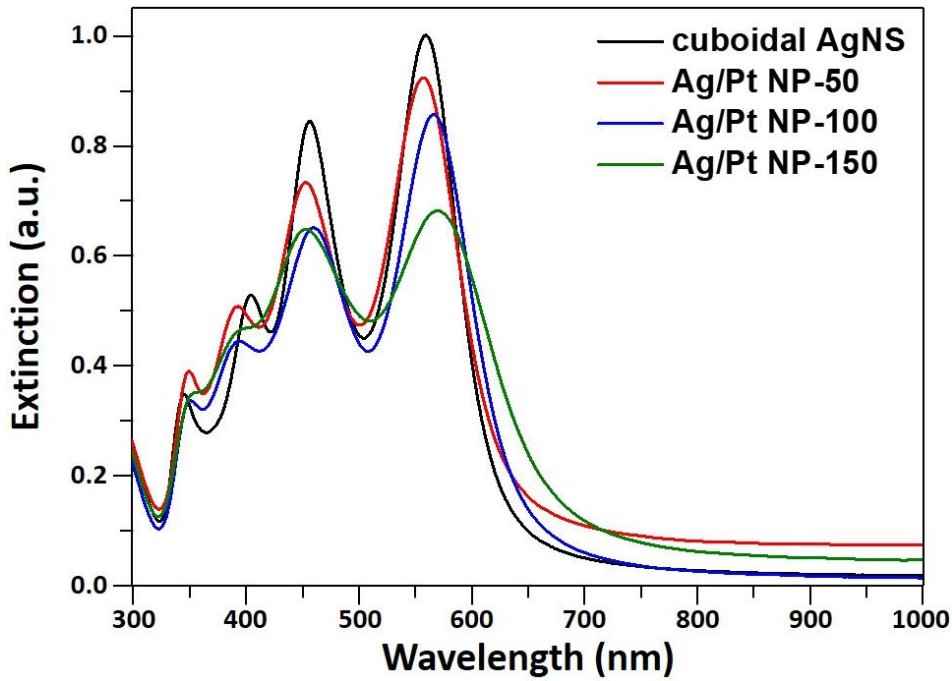

Figure 2.4. UV–Vis spectra of as-synthesized cuboidal AgNS and Ag/Pt NPs.

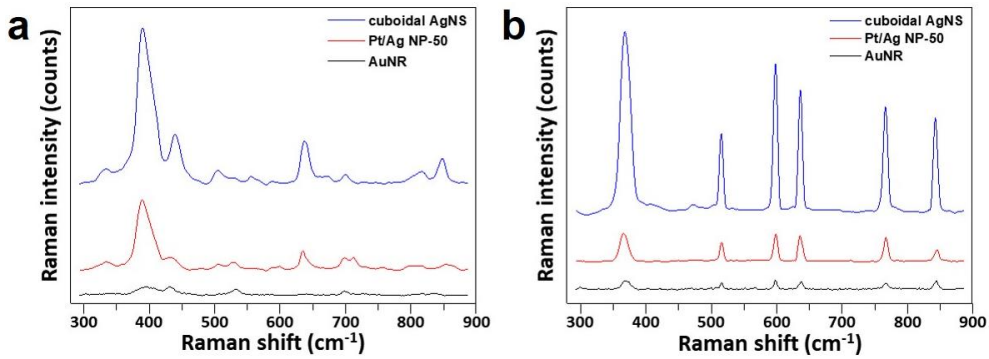

Figure 2.5. SERS spectra of (a) 4-ATP and (b) 2-NT decorated onto the surface of the as-synthesized AuNR, cuboidal AgNS, and Ag/Pt NP-50.

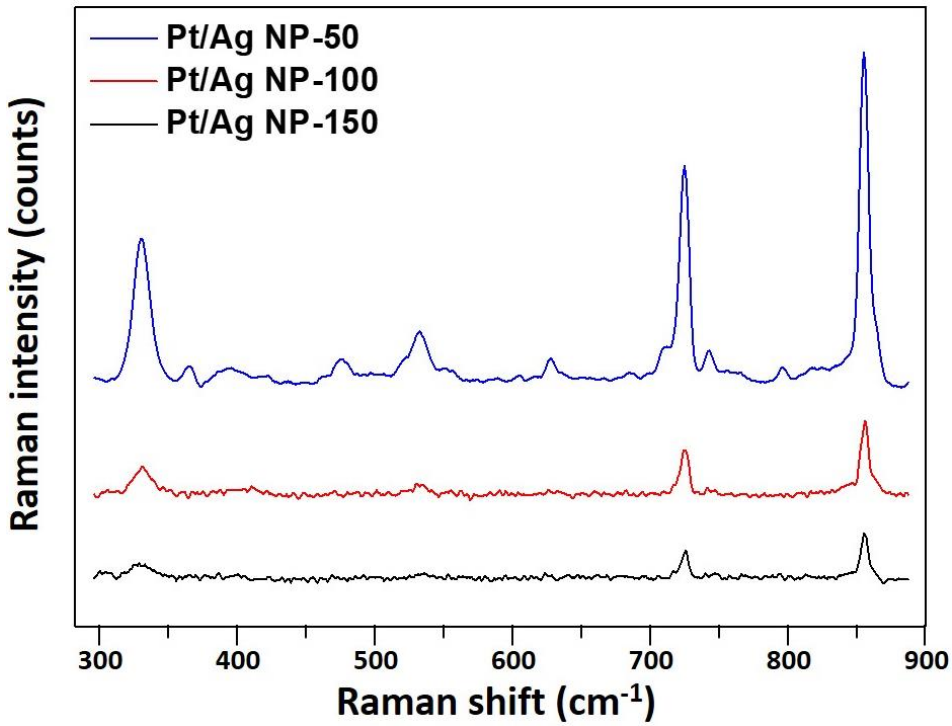

Figure 2.6. SERS spectra of 4-NPT decorated onto the surface of the as-synthesized Ag/Pt NPs depending on the substituted amount of Pt.

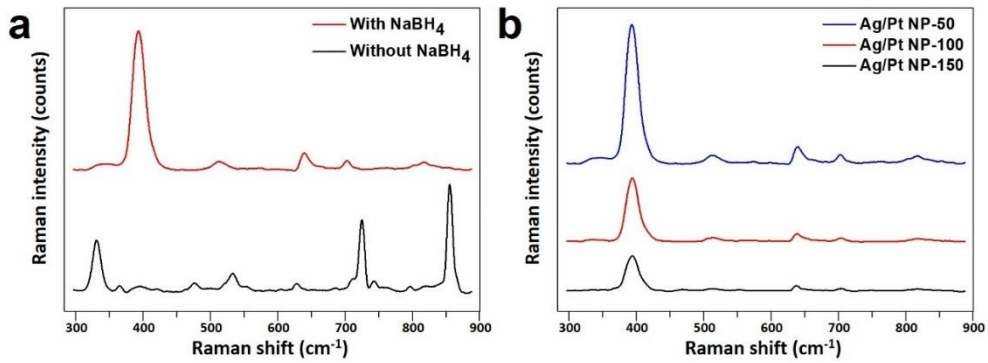

Figure 2.7. Catalytical chemical conversion from 4-NTP to 4-ATP on the surface of Ag/Pt NPs. (a) SERS spectra of 4-NTP before adding $NaBH_4$ solution to the Ag/Pt NP-50 (black spectra) and spectral changes from 4-NTP to 4-ATP at ten minutes after adding $NaBH_4$ solution (red spectra), which indicate the catalytic capability of as-synthesized bimetallic nanocatalysts (Ag/Pt NPs). (b) Catalytic chemical conversion of 4-NTP to 4-ATP on the surface of bimetallic nanocatalysts with different amount of Pt loading (Ag/Pt NP-50, 100, and 150).

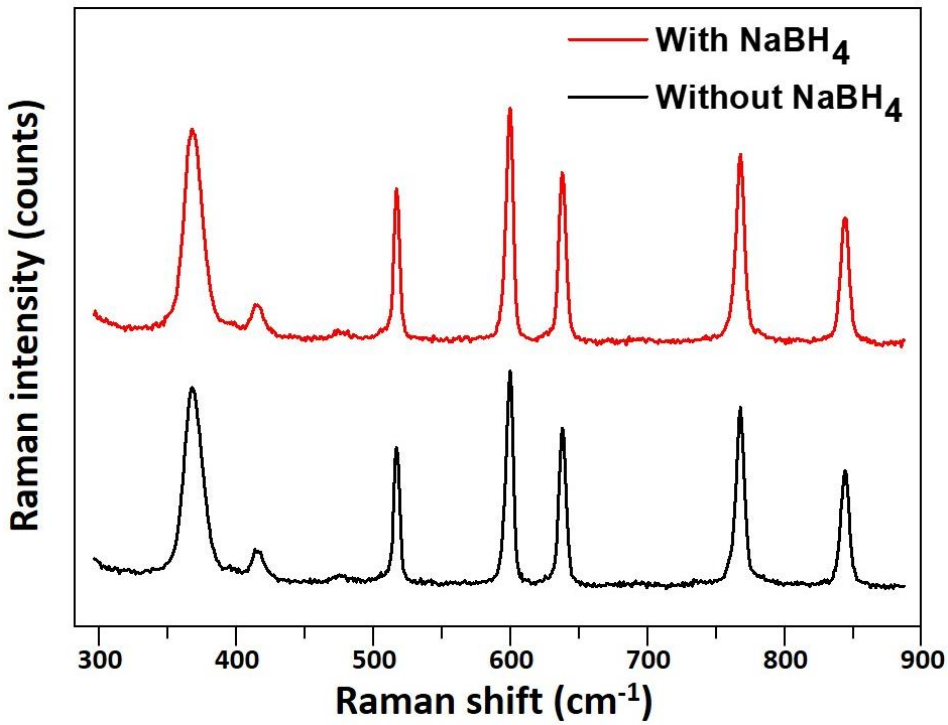

Figure 2.8. Chemical conversion of 2-NT on the surface of Ag/Pt NP-50 depending on the addition of $NaBH_4$ solution.

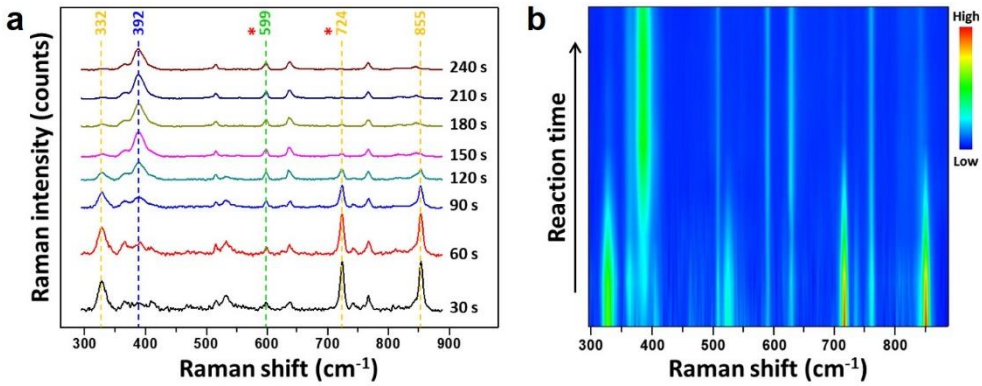

Figure 2.9. *In-situ* monitoring of catalytic chemical reaction by measuring spectral changes in Raman spectra for transformation from 4-NTP to 4-ATP under laser irradiation. (a) Time-dependent spectral changes of Raman molecules (i.e., from 4-NTP to 4-ATP) during catalytic chemical reaction. All the Raman spectra were acquired using 785 nm excitation laser at laser power density of 6.6×10^4 W/cm^2 and acquisition time of 5 s at every measurements. The orange-, blue-, and green-colored dashed line indicate the typical Raman peaks of 4-NTP, 4-ATP, and 2-NT, respectively. Whole Raman spectra were normalized using the intensity of the typical Raman peak of 2-NT (599 cm^{-1}). The red-colored asterisks indicate the typical Raman peaks of 4-NTP (724 cm^{-1}) and 2-NT (599 cm^{-1}) for calculating conversion rate constant (***k***) in Equation (1). (b) Color mapping of the spectral changes from 4-NTP to 4-ATP during catalytic chemical reaction using the spectra in **Figure 2.9**a.

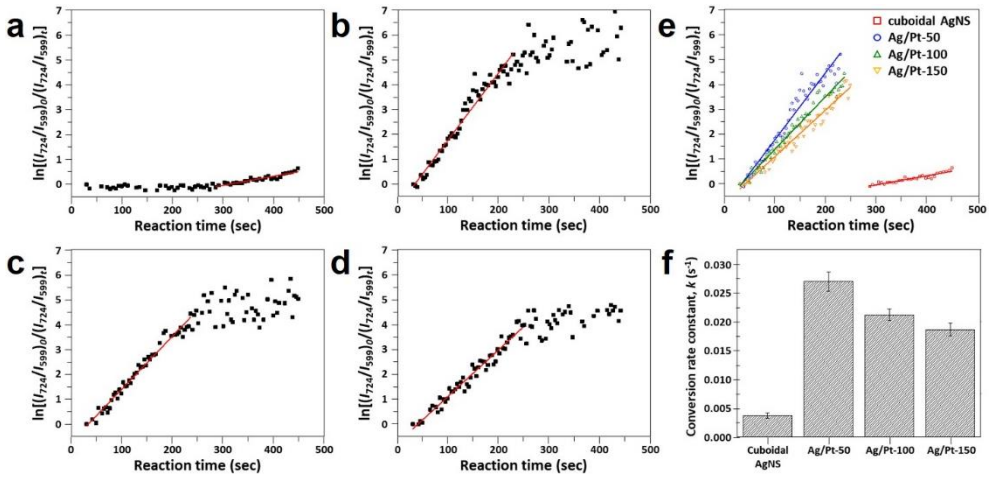

Figure 2.10. *In-situ* monitoring of catalytic chemical reaction occurred on the surface of as-synthesized nanocatalyts: (a) cuboidal AgNS, (b) Ag/Pt NP-50, (c) Ag/Pt NP-100, and (d) Ag/Pt NP-150. All the Raman spectra were acquired using 785 nm excitation laser at laser power density of 6.6 × 10^4 W/cm^2 and acquisition time of 2 s at every measurements with interval of 1 s between each measurements. (e) Plots of fitted curves during the catalytic chemical reaction. From the slopes obtained by plot between the logarithm of the relative Raman signal intensity (i.e., I_{724}/I_{599}) recorded at the beginning (***t***=0) and at certain measurement points (***t***) in the chemical reaction, the conversion rate constants (***k***) are calculated (i.e, gentle and steep slope indicate low and high ***k*** values, respectively). (f) Comparison of conversion rate constants (***k***) of cuboidal AgNS and Ag/Pt NPs with different amount of Pt loading.

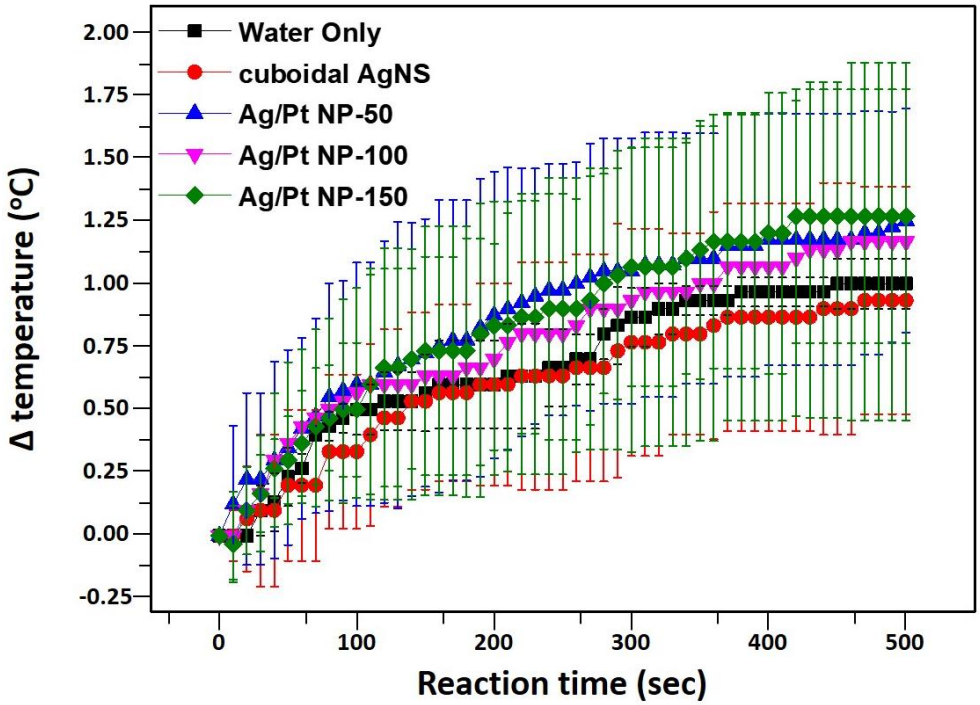

Figure 2.11. Time-dependent changes in the solution temperature of the as-synthesized nanocatalysts during the catalytic chemical reaction.

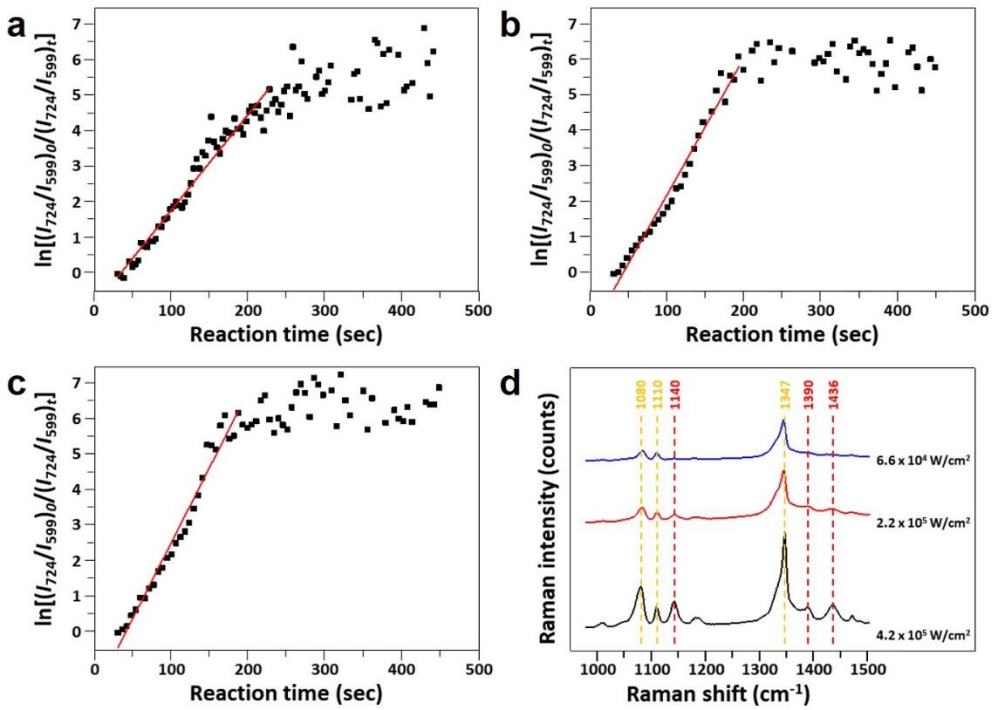

Figure 2.12. Catalytical chemical conversion from 4-NTP to 4-ATP on the surface of Ag/Pt NP-50 depending on the power density of irradiated laser: (a) 6.6 × 10^4 W/cm^2, (b) 2.2 × 10^5 W/cm^2, (c) 4.2 × 10^5 W/cm^2. All the Raman spectra were acquired using 785 nm excitation laser and acquisition time of 2 s at every measurements with interval of 1 s between each measurements. The higher power of the irradiated laser, the faster the chemical conversion rate. (d) Chemical transformation from 4-NTP (orange-colored dashed lines) to *p*,*p*'-dimercaptoazobenzene (DMAB; red-colored dashed lines) on the surface of Ag/Pt NP-50 under different power density of irradiated laser.

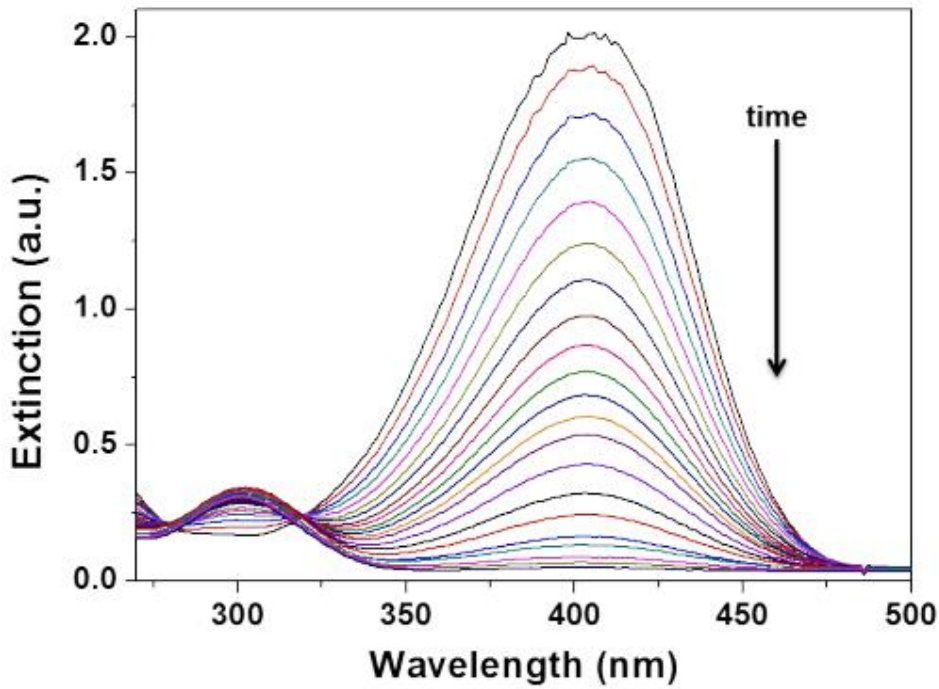

Figure 2.13. Time-dependent UV–Vis spectral changes of 4-NP in the presence of nanocatalysts. The natural extinction peak of 4-NP is strongly exhibited at λ = 317 nm, and shifts to λ = 400 nm after freshly prepared $NaBH_4$ solution is added, indicating the formation of 4-nitrophenolate ions. However, it gradually decreases in the presence of a nanocatalyst with a new extinction peak arising at λ = 300 nm, indicating conversion of 4-NP to 4-AP. During the successive decreases of the extinction peak at λ = 400 nm, two isosbestic points are visible at λ = 280 and 319 nm. These indicate that 4-NP was fully converted to 4-NP without side products in the catalytic reduction.

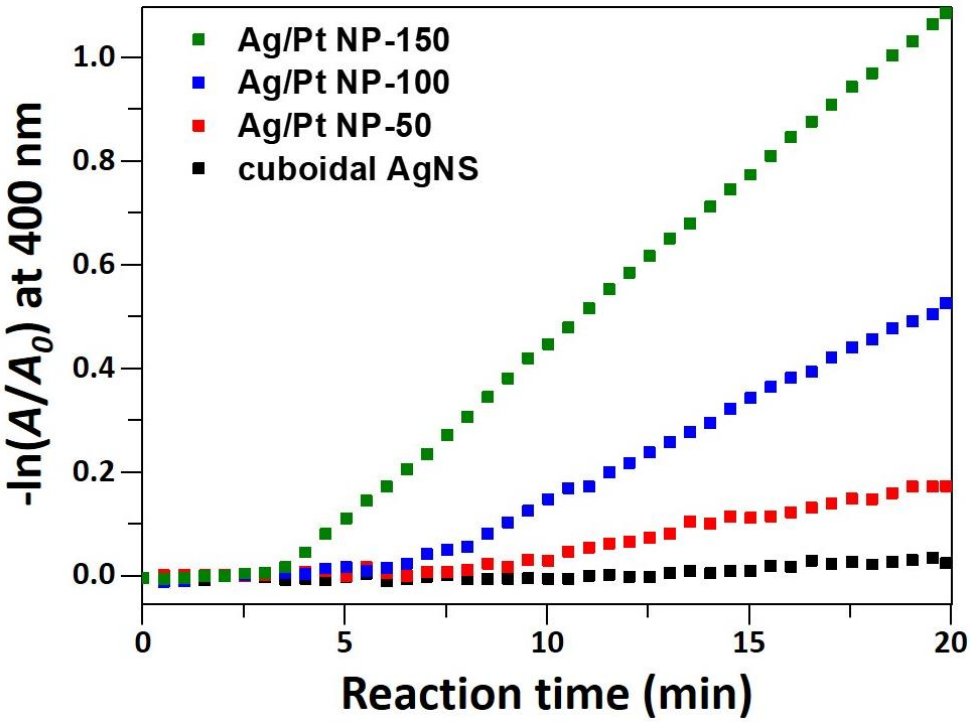

Figure 2.14. Catalytical chemical conversion from 4-NP to 4-AP on the surface of cuboidal AgNS and Ag/Pt NPs with different amount of Pt loading. Whole catalytic chemical reaction was monitored under the UV–Vis light irradiation in the presence of a freshly prepared $NaBH_4$ solution.

References

(1) Kim, M.; Ko, S. M.; Kim, J.-M.; Son, J.; Lee, C.; Rhim, W.-K.; Nam, J.-M. Dealloyed intra-nanogap particles with highly robust, quantifiable surface-enhanced Raman scattering signals for biosensing and bioimaging applications. *ACS Central Science* **2018**, *4*, 277–287.

(2) Kumar, A.; Kim, S.; Nam, J.-M. Plasmonically engineered nanoprobes for biomedical applications. *Journal of the American Chemical Society* **2016**, *138*, 14509–14525.

(3) Park, J.-E.; Jung, Y.; Kim, M.; Nam, J.-M. Quantitative nanoplasmonics. *ACS Central Science* **2018**, *4*, 1303–1314.

(4) Anker, J. N.; Hall, W. P.; Lyandres, O.; Shah, N. C.; Zhao, J.; Van Duyne, R. P. Biosensing with plasmonic nanosensors. *Nature Materials* **2008**, *7*, 442–453.

(5) Orendorff, C. J.; Gole, A.; Sau, T. K.; Murphy, C. J. Surface-enhanced Raman spectroscopy of self-assembled monolayers: sandwich architecture and nanoparticle shape dependence. *Analytical Chemistry* **2005**, *77*, 3261–3266.

(6) Nie, S.; Emory, S. R. Probing single molecules and single nanoparticles by surface-enhanced Raman scattering. *Science* **1997**, *275*, 1102–1106.

(7) Lee, C.; Robertson, C. S.; Nguyen, A. H.; Kahraman, M.; Wachsmann-Hogiu, S. Thickness of a metallic film, in addition to its roughness,

plays a significant role in SERS activity. *Scientific Reports* **2015**, *5*, 11644.

(8) Yang, Y.; Shi, J.; Kawamura, G.; Nogami, M. Preparation of Au–Ag, Ag–Au core–shell bimetallic nanoparticles for surface-enhanced Raman scattering. *Scripta Materialia* **2008**, *58*, 862–865.

(9) Indrasekara, A. S. D. S.; Meyers, S.; Shubeita, S.; Feldman, L. C.; Gustafsson, T.; Fabris, L. Gold nanostar substrates for SERS-based chemical sensing in the femtomolar regime. *Nanoscale* **2014**, *6*, 8891–8899.

(10) Liu, K.; Bai, Y.; Zhang, L.; Yang, Z.; Fan, Q.; Zheng, H.; Yin, Y.; Gao, C. Porous Au–Ag nanospheres with high-density and highly accessible hotspots for SERS analysis. *Nano Letters* **2016**, *16*, 3675–3681.

(11) Lee, J.-H.; You, M.-H.; Kim, G.-H.; Nam, J.-M. Plasmonic nanosnowmen with a conductive junction as highly tunable nanoantenna structures and sensitive, quantitative and multiplexable surface-enhanced Raman scattering probes. *Nano Letters* **2014**, *14*, 6217–6225.

(12) Nam, J.-M.; Oh, J.-W.; Lee, H.; Suh, Y. D. Plasmonic nanogap-enhanced Raman scattering with nanoparticles. *Accounts of Chemical Research* **2016**, *49*, 2746–2755.

(13) Shanthil, M.; Thomas, R.; Swathi, R. S.; George Thomas, K. Ag@SiO_2 core–shell nanostructures: distance-dependent plasmon coupling and SERS investigation. *The Journal of Physical Chemistry Letters* **2012**, *3*, 1459–1464.

(14) Shao, F.; Lu, Z.; Liu, C.; Han, H.; Chen, K.; Li, W.; He, Q.; Peng, H.; Chen, J. Hierarchical nanogaps within bioscaffold arrays as a high-performance SERS substrate for animal virus biosensing. *ACS Applied Materials & Interfaces* **2014**, *6*, 6281–6289.

(15) Chen, X.; Guo, Z.; Yang, G.-M.; Li, J.; Li, M.-Q.; Liu, J.-H.; Huang, X.-J. Electrical nanogap devices for biosensing. *Materials Today* **2010**, *13*, 28–41.

(16) Fraire, J. C.; Pérez, L. A.; Coronado, E. A. Rational design of plasmonic nanostructures for biomolecular detection: Interplay between theory and experiments. *ACS Nano* **2012**, *6*, 3441–3452.

(17) Xu, L.; Yan, W.; Ma, W.; Kuang, H.; Wu, X.; Liu, L.; Zhao, Y.; Wang, L.; Xu, C. SERS encoded silver pyramids for attomolar detection of multiplexed disease biomarkers. *Advanced Materials* **2015**, *27*, 1706–1711.

(18) Zhao, B.; Shen, J.; Chen, S.; Wang, D.; Li, F.; Mathur, S.; Song, S.; Fan, C. Gold nanostructures encoded by non-fluorescent small molecules in polyA-mediated nanogaps as universal SERS nanotags for recognizing various bioactive molecules. *Chemical Science* **2014**, *5*, 4460–4466.

(19) Zhou, J.; Xiong, Q.; Ma, J.; Ren, J.; Messersmith, P. B.; Chen, P.; Duan, H. Polydopamine-enabled approach toward tailored plasmonic nanogapped nanoparticles: From nanogap engineering to multifunctionality. *ACS Nano* **2016**, *10*, 11066–11075.

(20) Su, J.; Wang, D.; Nörbel, L.; Shen, J.; Zhao, Z.; Dou, Y.; Peng, T.; Shi, J.; Mathur, S.; Fan, C.; Song, S. Multicolor gold–silver nano-

mushrooms as ready-to-use SERS probes for ultrasensitive and multiplex DNA/miRNA detection. *Analytical Chemistry* **2017**, *89*, 2531–2538.

(21) Hatab, N. A.; Hsueh, C.-H.; Gaddis, A. L.; Retterer, S. T.; Li, J.-H.; Eres, G.; Zhang, Z.; Gu, B. Free-standing optical gold bowtie nanoantenna with variable gap size for enhanced Raman spectroscopy. *Nano Letters* **2010**, *10*, 4952–4955.

(22) Lim, D.-K.; Jeon, K.-S.; Hwang, J.-H.; Kim, H.; Kwon, S.; Suh, Y. D.; Nam, J.-M. Highly uniform and reproducible surface-enhanced Raman scattering from DNA-tailorable nanoparticles with 1-nm interior gap. *Nature Nanotechnology* **2011**, *6*, 452–460.

(23) Oh, J.-W.; Lim, D.-K.; Kim, G.-H.; Suh, Y. D.; Nam, J.-M. Thiolated DNA-based chemistry and control in the structure and optical properties of plasmonic nanoparticles with ultrasmall interior nanogap. *Journal of the American Chemical Society* **2014**, *136*, 14052–14059.

(24) Tan, S. J.; Campolongo, M. J.; Luo, D.; Cheng, W. Building plasmonic nanostructures with DNA. *Nature Nanotechnology* **2011**, *6*, 268–276.

(25) Lim, D.-K.; Jeon, K.-S.; Kim, H. M.; Nam, J.-M.; Suh, Y. D. Nanogap-engineerable Raman-active nanodumbbells for single-molecule detection. *Nature Materials* **2010**, *9*, 60–67.

(26) Lee, J.-H.; Nam, J.-M.; Jeon, K.-S.; Lim, D.-K.; Kim, H.; Kwon, S.; Lee, H.; Suh, Y. D. Tuning and maximizing the single-molecule surface-enhanced Raman scattering from DNA-tethered nanodumbbells. *ACS Nano* **2012**, *6*, 9574–9584.

(27) Chen, H.; Sun, Z.; Ni, W.; Woo, K. C.; Lin, H.-Q.; Sun, L.; Yan, C.; Wang, J. Plasmon coupling in clusters composed of two-dimensionally ordered gold nanocubes. *Small* **2009**, *5*, 2111–2119.

(28) Park, J.-E.; Lee, Y.; Nam, J.-M. Precisely Shaped, Uniformly Formed Gold Nanocubes with Ultrahigh Reproducibility in Single-Particle Scattering and Surface-Enhanced Raman Scattering. *Nano Letters* **2018**, *18*, 6475–6482.

(29) Zheng, Y.; Zhong, X.; Li, Z.; Xia, Y. Successive, seed-mediated growth for the synthesis of single-crystal gold nanospheres with uniform diameters controlled in the range of 5–150 nm. *Particle & Particle Systems Characterization* **2014**, *31*, 266–273.

(30) Park, K.; Koerner, H.; Vaia, R. A. Depletion-induced shape and size selection of gold nanoparticles. *Nano Letters* **2010**, *10*, 1433–1439.

(31) Hurst, S. J.; Lytton-Jean, A. K. R.; Mirkin, C. A. Maximizing DNA loading on a range of gold nanoparticle sizes. *Analytical Chemistry* **2006**, *78*, 8313–8318.

(32) Hohenester, U.; Trügler, A. MNPBEM – A Matlab toolbox for the simulation of plasmonic nanoparticles. *Computer Physics Communications* **2012**, *183*, 370–381.

(33) Hohenester, U. Simulating electron energy loss spectroscopy with the MNPBEM toolbox. *Computer Physics Communications* **2014**, *185*, 1177–1187.

(34) Waxenegger, J.; Trügler, A.; Hohenester, U. Plasmonics simulations with the MNPBEM toolbox: Consideration of substrates and layer structures. *Computer Physics Communications* **2015**, *193*, 138–150.

(35) Johnson, P. B.; Christy, R. W. Optical constants of the noble metals. *Physical Review B* **1972**, *6*, 4370–4379.

(36) Lal, S.; Grady, N. K.; Kundu, J.; Levin, C. S.; Lassiter, J. B.; Halas, N. J. Tailoring plasmonic substrates for surface enhanced spectroscopies. *Chemical Society Reviews* **2008**, *37*, 898–911.

(37) Banholzer, M. J.; Millstone, J. E.; Qin, L.; Mirkin, C. A. Rationally designed nanostructures for surface-enhanced Raman spectroscopy. *Chemical Society Reviews* **2008**, *37*, 885–897.

(38) Camden, J. P.; Dieringer, J. A.; Zhao, J.; Van Duyne, R. P. Controlled plasmonic nanostructures for surface-enhanced spectroscopy and sensing. *Accounts of Chemical Research* **2008**, *41*, 1653–1661.

(39) Park, H.-G.; Joo, J. H.; Kim, H.-G.; Lee, J.-S. Shape-dependent reversible assembly properties of polyvalent DNA–silver nanocube conjugates. *The Journal of Physical Chemistry C* **2012**, *116*, 2278–2284.

(40) Elghanian, R.; Storhoff, J. J.; Mucic, R. C.; Letsinger, R. L.; Mirkin, C. A. Selective colorimetric detection of polynucleotides based on the distance-dependent optical properties of gold nanoparticles. *Science* **1997**, *277*, 1078–1081.

(41) Taton, T. A.; Mirkin, C. A.; Letsinger, R. L. Scanometric DNA array detection with nanoparticle probes. *Science* **2000**, *289*, 1757–1760.

(42) Hurst, S. J.; Hill, H. D.; Mirkin, C. A. "Three-dimensional hybridization" with polyvalent DNA−gold nanoparticle conjugates. *Journal of the American Chemical Society* **2008**, *130*, 12192–12200.

(43) Jin, R.; Wu, G.; Li, Z.; Mirkin, C. A.; Schatz, G. C. What controls the melting properties of DNA-linked gold nanoparticle assemblies? *Journal of the American Chemical Society* **2003**, *125*, 1643–1654.

(44) Esteban, R.; Aguirregabiria, G.; Borisov, A. G.; Wang, Y. M.; Nordlander, P.; Bryant, G. W.; Aizpurua, J. The morphology of narrow gaps modifies the plasmonic response. *ACS Photonics* **2015**, *2*, 295–305.

(45) Pellarin, M.; Ramade, J.; Rye, J. M.; Bonnet, C.; Broyer, M.; Lebeault, M.-A.; Lermé, J.; Marguet, S.; Navarro, J. R. G.; Cottancin, E. Fano transparency in rounded nanocube dimers induced by gap plasmon coupling. *ACS Nano* **2016**, *10*, 11266–11279.

(46) Kim, M.; Lee, C.; Ko, S. M.; Nam, J.-M. Metal alloy hybrid nanoparticles with enhanced catalytic activities in fuel cell applications. *Journal of Solid State Chemistry* **2019**, *270*, 295-303.

(47) Stamenkovic, V.; Mun, B. S.; Mayrhofer, K. J. J.; Ross, P. N.; Markovic, N. M.; Rossmeisl, J.; Greeley, J.; Nørskov, J. K. Changing the activity of electrocatalysts for oxygen reduction by tuning the surface electronic structure. *Angewandte Chemie International Edition* **2006**, *45*, 2897-2901.

(48) Chen, C.; Kang, Y.; Huo, Z.; Zhu, Z.; Huang, W.; Xin, H. L.; Snyder, J. D.; Li, D.; Herron, J. A.; Mavrikakis, M.; Chi, M.; More, K. L.; Li, Y.; Markovic, N. M.; Somorjai, G. A.; Yang, P.; Stamenkovic, V. R. Highly crystalline multimetallic nanoframes with three-dimensional electrocatalytic surfaces. *Science* **2014**, *343*, 1339-1343.

(49) Huang, X.; Zhao, Z.; Cao, L.; Chen, Y.; Zhu, E.; Lin, Z.; Li, M.; Yan, A.; Zettl, A.; Wang, Y. M.; Duan, X.; Mueller, T.; Huang, Y. High-performance transition metal–doped Pt_3Ni octahedra for oxygen reduction reaction. *Science* **2015**, *348*, 1230-1234.

(50) Wang, H.; Jusys, Z.; Behm, R. J. Ethanol electrooxidation on a Carbon-supported Pt catalyst: reaction kinetics and product yields. *The Journal of Physical Chemistry B* **2004**, *108*, 19413-19424.

(51) Antolini, E.; Salgado, J. R. C.; Gonzalez, E. R. The stability of Pt–M (M=first row transition metal) alloy catalysts and its effect on the activity in low temperature fuel cells: A literature review and tests on a Pt–Co catalyst. *Journal of Power Sources* **2006**, *160*, 957-968.

(52) Liao, H.; Fisher, A.; Xu, Z. J. Surface segregation in bimetallic nanoparticles: A critical issue in electrocatalyst engineering. *Small* **2015**, *11*, 3221-3246.

(53) Zhang, B.-W.; Yang, H.-L.; Wang, Y.-X.; Dou, S.-X.; Liu, H.-K. A comprehensive review on controlling surface composition of Pt-based bimetallic electrocatalysts. *Advanced Energy Materials* **2018**, *8*, 1703597.

(54) Jang, J.-H.; Lee, E.; Park, J.; Kim, G.; Hong, S.; Kwon, Y.-U. Rational syntheses of core-shell Fe_x@Pt nanoparticles for the study of electrocatalytic oxygen reduction reaction. *Scientific Reports* **2013**, *3*, 2872.

(55) Bu, L.; Guo, S.; Zhang, X.; Shen, X.; Su, D.; Lu, G.; Zhu, X.; Yao, J.; Guo, J.; Huang, X. Surface engineering of hierarchical platinum-

cobalt nanowires for efficient electrocatalysis. *Nature Communications* **2016**, *7*, 11850.

(56) Zou, L.; Fan, J.; Zhou, Y.; Wang, C.; Li, J.; Zou, Z.; Yang, H. Conversion of PtNi alloy from disordered to ordered for enhanced activity and durability in methanol-tolerant oxygen reduction reactions. *Nano Research* **2015**, *8*, 2777-2788.

(57) Kulkarni, A.; Siahrostami, S.; Patel, A.; Nørskov, J. K. Understanding catalytic activity trends in the oxygen reduction reaction. *Chemical Reviews* **2018**, *118*, 2302-2312.

(58) Ontaneda, J.; Bennett, R. A.; Grau-Crespo, R. Electronic structure of Pd multilayers on Re(0001): The role of charge transfer. *The Journal of Physical Chemistry C* **2015**, *119*, 23436-23444.

(59) Mistry, H.; Varela, A. S.; Kühl, S.; Strasser, P.; Cuenya, B. R. Nanostructured electrocatalysts with tunable activity and selectivity. *Nature Reviews Materials* **2016**, *1*, 16009.

(60) Mavrikakis, M.; Hammer, B.; Nørskov, J. K. Effect of strain on the reactivity of metal surfaces. *Physical Review Letters* **1998**, *81*, 2819-2822.

(61) Kim, M.; Lin, M.; Son, J.; Xu, H.; Nam, J.-M. Hot-electron-mediated photochemical reactions: Principles, recent ddvances, and challenges. *Advanced Optical Materials* **2017**, *5*, 1700004.

(62) Kim, M.; Lee, J.-H.; Nam, J.-M. Plasmonic photothermal nanoparticles for biomedical applications. *Advanced Science* **2019**, *6*, 1900471.

(63) Polo, E.; Navarro Poupard, M. F.; Guerrini, L.; Taboada, P.; Pelaz, B.; Alvarez-Puebla, R. A.; del Pino, P. Colloidal bioplasmonics. *Nano Today* **2018**, *20*, 58-73.

(64) Brongersma, M. L.; Halas, N. J.; Nordlander, P. Plasmon-induced hot carrier science and technology. *Nature Nanotechnology* **2015**, *10*, 25-34.

(65) Knight, M. W.; Sobhani, H.; Nordlander, P.; Halas, N. J. Photodetection with Active Optical Antennas. *Science* **2011**, *332*, 702-704.

(66) Atar, F. B.; Battal, E.; Aygun, L. E.; Daglar, B.; Bayindir, M.; Okyay, A. K. Plasmonically enhanced hot electron based photovoltaic device. *Optics Express* **2013**, *21*, 7196-7201.

(67) Mubeen, S.; Lee, J.; Singh, N.; Krämer, S.; Stucky, G. D.; Moskovits, M. An autonomous photosynthetic device in which all charge carriers derive from surface plasmons. *Nature Nanotechnology* **2013**, *8*, 247-251.

(68) Fang, Y.; Li, Y.; Xu, H.; Sun, M. Ascertaining p,p′-dimercaptoazobenzene produced from p-aminothiophenol by selective catalytic coupling reaction on silver nanoparticles. *Langmuir* **2010**, *26*, 7737-7746.

(69) Mukherjee, S.; Libisch, F.; Large, N.; Neumann, O.; Brown, L. V.; Cheng, J.; Lassiter, J. B.; Carter, E. A.; Nordlander, P.; Halas, N. J. Hot electrons do the impossible: Plasmon-induced dissociation of H2 on Au. *Nano Letters* **2013**, *13*, 240-247.

(70) Wang, F.; Li, C.; Chen, H.; Jiang, R.; Sun, L.-D.; Li, Q.; Wang, J.; Yu, J. C.; Yan, C.-H. Plasmonic harvesting of light energy for Suzuki coupling reactions. *Journal of the American Chemical Society* **2013**, *135*, 5588-5601.

(71) Zheng, Z.; Tachikawa, T.; Majima, T. Single-particle study of Pt-modified Au nanorods for plasmon-enhanced hydrogen generation in visible to near-infrared region. *Journal of the American Chemical Society* **2014**, *136*, 6870-6873.

(72) Mori, K.; Kawashima, M.; Che, M.; Yamashita, H. Enhancement of the photoinduced oxidation activity of a Ruthenium(II) complex anchored on silica-coated silver nanoparticles by localized surface plasmon resonance. *Angewandte Chemie International Edition* **2010**, *49*, 8598-8601.

(73) Nikoobakht, B.; El-Sayed, M. A. Preparation and Growth Mechanism of Gold Nanorods (NRs) Using Seed-Mediated Growth Method. *Chemistry of Materials* **2003**, *15*, 1957-1962.

(74) Park, K.; Drummy, L. F.; Vaia, R. A. Ag Shell Morphology on Au Nanorod Core: Role of Ag Precursor Complex. *Journal of Materials Chemistry* **2011**, *21*, 15608-15618.

(75) Sun, Y.; Xia, Y. Mechanistic study on the replacement reaction between silver nanostructures and chloroauric acid in aqueous medium. *Journal of the American Chemical Society* **2004**, *126*, 3892-3901.

(76) Lin, S.-C.; Hsu, C.-S.; Chiu, S.-Y.; Liao, T.-Y.; Chen, H. M. Edgeless Ag–Pt bimetallic nanocages: In Situ monitor plasmon-induced

suppression of hydrogen peroxide formation. *Journal of the American Chemical Society* **2017**, *139*, 2224-2233.

(77) Kim, M.; Lin, M.; Son, J.; Xu, H.; Nam, J.-M. Hot-Electron-Mediated Photochemical Reactions: Principles, Recent Advances, and Challenges. *Advanced Optical Materials* **2017**, *5*, 1700004.

(78) Xie, W.; Herrmann, C.; Kömpe, K.; Haase, M.; Schlücker, S. Synthesis of bifunctional Au/Pt/Au core/shell nanoraspberries for in Situ SERS monitoring of platinum-catalyzed reactions. *Journal of the American Chemical Society* **2011**, *133*, 19302-19305.

(79) Ren, X.; Tan, E.; Lang, X.; You, T.; Jiang, L.; Zhang, H.; Yin, P.; Guo, L. Observing reduction of 4-nitrobenzenthiol on gold nanoparticles in Situ using surface-enhanced Raman spectroscopy. *Physical Chemistry Chemical Physics* **2013**, *15*, 14196-14201.

(80) Saha, S.; Pal, A.; Kundu, S.; Basu, S.; Pal, T. Photochemical green synthesis of calcium-alginate-stabilized Ag and Au nanoparticles and their catalytic application to 4-nitrophenol reduction. *Langmuir* **2010**, *26*, 2885-2893.

(81) Joseph, V.; Engelbrekt, C.; Zhang, J.; Gernert, U.; Ulstrup, J.; Kneipp, J. Characterizing the kinetics of nanoparticle-catalyzed reactions by surface-enhanced Raman scattering. *Angewandte Chemie International Edition* **2012**, *51*, 7592-7596.

(82) Khalavka, Y.; Becker, J.; Sönnichsen, C. Synthesis of rod-shaped gold nanorattles with improved plasmon sensitivity and catalytic activity. *Journal of the American Chemical Society* **2009**, *131*, 1871-1875.

(83) Skadtchenko, B. O.; Aroca, R. Surface-enhanced Raman scattering of p-nitrothiophenol: Molecular vibrations of its silver salt and the surface complex formed on silver islands and colloids. *Spectrochimica Acta Part A: Molecular and Biomolecular Spectroscopy* **2001**, *57*, 1009-1016.

(84) Alvarez-Puebla, R. A.; Dos Santos Jr, D. S.; Aroca, R. F. Surface-enhanced Raman scattering for ultrasensitive chemical analysis of 1 and 2-naphthalenethiols. *Analyst* **2004**, *129*, 1251-1256.

(85) Kang, L.; Xu, P.; Zhang, B.; Tsai, H.; Han, X.; Wang, H.-L. Laser wavelength- and power-dependent plasmon-driven chemical reactions monitored using single particle surface enhanced Raman spectroscopy. *Chemical Communications* **2013**, *49*, 3389-3391.

(86) Dong, B.; Fang, Y.; Chen, X.; Xu, H.; Sun, M. Substrate-, wavelength-, and time-dependent plasmon-assisted surface catalysis reaction of 4-nitrobenzenethiol dimerizing to p,p′-dimercaptoazobenzene on Au, Ag, and Cu films. *Langmuir* **2011**, *27*, 10677-10682.

(87) Kim, M.; Ko, S. M.; Nam, J.-M. Dealloying-based facile synthesis and highly catalytic properties of Au core/porous shell nanoparticles. *Nanoscale* **2016**, *8*, 11707-11717.

(88) Zheng, G.; Polavarapu, L.; Liz-Marzán, L. M.; Pastoriza-Santos, I.; Pérez-Juste, J. Gold nanoparticle-loaded filter paper: A recyclable dip-catalyst for real-time reaction monitoring by surface enhanced Raman scattering. *Chemical Communications* **2015**, *51*, 4572-4575.

요약 (국문초록)

광학적 및 화학적 특성이 향상된 귀금속 나노구조체의 플라즈모닉 특성 연구와 이의 표면증강라만산란 기반 바이오분석 및 촉매화학 반응 응용

표면 강화 라만 산란(SERS)은 금, 은, 구리 등의 귀금속 나노 구조 표면 근처에 전자기장을 강하게 향상시킬 수 있는 독특한 특성으로 인해 큰 주목을 받고 있다. 또한 SERS 기술은 광학 신호의 감도, 선택성, 다중성, 안정성 등에 있어서 뛰어난 장점이 있기 때문에 화학 및 생물학적 검지/이미징 응용 분야에 매우 유망한 기술이다. 귀금속 나노 구조에 의한 전자기장의 강한 증강 현상은 단일 분자를 검지 할 수 있을 만큼 매우 민감한 검출 한계를 나타낼 수 있으며, 이러한 플라즈모닉 특성은 금속 나노구조체의 크기, 모양, 구성, 재료 등에 따라 조절될 수 있다. 특히, 금속 나노구조체 간 나노 미터 크기의 작은 갭이 형성되면, 플라즈모닉 커플링 현상에 의해 전체 전자기장이 크게 증폭될 수 있다. 이러한 이유로, 금속 나노구조체 간

나노 갭을 형성시킴으로써 플라즈모닉 나노 구조체 주변의 전자기장을 크게 증폭시키고 이를 여러 분야에 활용하기 위한 많은 시도가 있었으나, SERS 신호를 강하게 증폭시키면서도 나노 구조를 정밀하게 조립하고 나노 갭을 균일하게 제어하는 기술은 특히 광학 신호의 정량적 측면에서 여전히 매우 도전적이다.

플라즈모닉 나노 구조체 표면 근처에 전자기장을 강하고 균일하게 증폭시키려는 목적과 함께, 레이저 조사 하에서 플라즈모닉 나노 구조체의 화학적 특성을 강하게 향상시키기 위한 연구 또한 집중적으로 수행되고 있다. 표면 플라즈몬의 비방사성 쇠퇴 과정을 통해 생성된 고에너지의 열전자가 금속 나노입자 표면에 인접한 반응물로 전달 되면 전체 화학 반응의 효율과 선택성이 촉진되거나 향상될 수 있다. 지금까지 고에너지의 열전자가 다양한 화학 반응에 참여할 수 있으며 그 결과 화학 반응의 효율을 향상시킬 수 있다는 사실이 많은 연구들을 통해 입증되었지만, 열전자가 촉매 화학 반응 속도를 얼마나 빠르게 향상시키는지에 대한 정량적이고 동역학적인 분석은 아직 거의 이루어지지 않았다.

본 학위 논문에서는, 귀금속 나노구조체의 플라즈모닉 특성을 활용하여 광학적 및 화학적 특성을 향상시키는 연구 결과들을 제시하였다. 금 나노큐브를 계층적으로 조립하여 금 나노큐브 계면에서 발생되는 플라즈모닉 커플링 현상에 의한 광학 신호 증강 효과를 통해 SERS 신호 기반의 핵산 검지능의 향상을 분석하였고, 은과 백금으로 구성된 이중금속 나노 합금 입자를 이용하여 촉매 화학 반응 실시간 모니터링 수행 및 촉매 특성 향상을 통한 전환율 상수의 개선 효과를 정량적으로 분석하였다.

1 장에서는, 금 나노큐브를 계층적으로 조립하여 나노큐브 간 계면에서 발생하는 전자기장 증폭 효과를 제어하고, 이를 SERS 신호 기반의 핵산 검지 플랫폼에 적용하였다. 이러한 접근법을 통해, 검지하고자 하는 표적 핵산을 100 aM 에서 10 pM 농도까지 넓은 범위에 걸쳐 재현 가능한 방식으로 안정적으로 표적 핵산을 검지하였다. 특히, 나노입자 표면 형태의 차이에 기인하여, 평평한 표면을 가진 금 나노큐브 구조체는 구부러진 표면을 가진 구형 금 나노입자에 비해 더 빠르고 강하게 결합을 이루고, 결합된 금 나노큐브 조립체는 더 넓은 범위에 걸쳐 안정적이고 강하게

전자기장을 증폭시킬 수 있었다. 이러한 구조적인 특성에 의해 매우 민감하고 정량적인 바이오 검출 분석/분석이 가능하였다.

2 장에서는, SERS 신호 기반으로 촉매 화학 반응을 실시간 모니터링할 수 있도록 은과 백금으로 구성된 이중금속 나노입자를 합성하고, 플라즈모닉 특성에 의한 촉매 화학 반응의 향상을 분석하였다. 과학/플라즈몬 특성과 촉매 특성을 단일 나노 구조에서 동시에 구현하는 이중금속 나노입자를 형성하기 위하여 입방체 은 나노구조와 백금 이온간의 갈바닉 치환 반응을 이용하였으며, 갈바닉 치환 반응의 정도를 제어함으로써 은과 백금의 원자 비가 다양하게 조절된 나노촉매 입자를 합성하였다. 흥미롭게도, 은/백금 이중금속 나노촉매는 레이저 조명 하에서 백금의 양이 적을수록 화학반응이 더 빨라지는 독특한 광학 특성을 보였다. 이러한 특이적인 촉매 특성 경향은, 우수한 플라즈모닉 특성을 보이는 은 금속으로부터 발생한 고에너지의 열전자가 인접한 반응물에 전달됨으로 인해 전체 화학반응의 속도가 빨라진 것이라 예상한다. 이는, 열전자의 생성 및 주입이 추가 전자 공급원으로써 전체 촉매 화학 반응에 크기 기여할

수 있으며, 백금을 최소한으로 사용하더라도 촉매 전환율 상수를 크게 개설할 수 있다는 것을 시사한다.

종합적으로 본 학위 논문에서의 연구 결과들은, 정량적이고 고민감도로 SERS 신호 기반의 표적 분자 검지 플랫폼을 활용할 수 있는 방법을 제시하고, 고효율의 이중금속 광촉매 디자인 및 다목적의 열전자 공학 설계의 길을 열어줍니다.

주요어: 플라즈모닉스, 표면 증강 라만 산란, 금 나노큐브, 핵산, 계층적 조립, SERS 신호 기반 바이오검지, 열전자, 은/백금 이중금속 나노구조체, 갈바닉 치환 반응, 촉매 화학 반응 모니터링, 동역학적 분석, 전환율 향상.

학번: 2015-30975